University of Leeds

The Mechanism of Formation of Porous Calcite Composite Crystals Through Thermal Decomposition

[redacted]

Supervisors: [redacted]

Final Year Project

17/05/2013

Student ID: [redacted]

Acknowledgements

I would like to thank [redacted] for her tremendous amount of time and help throughout this project and [redacted] for providing this opportunity for me. [redacted] and [redacted] for their continual support throughout my Nanotechnology BSc. My Mum, the most reliable and important person in my life, for everything you have ever done for me. My Dad, for generating my love of science at a young age. My brother and sisters, Alexander, Aurelia and Aprillia.

Abstract

Calcite biominerals, such as sea urchin shells, are intricately controlled inorganic-organic composites with well defined structures and morphologies, with various organic occlusions within a single crystal. In this work, calcite composite single crystals were synthesized by employing the ammonium diffusion method. A novel approach to create porosity controlled calcite single crystals by a one-step thermal decomposition was investigated. The calcite crystals were precipitated in the presence of aspartic acid or glycine resulting in their occlusion throughout the crystal; a change in morphology depending on the concentration of the additives was observed. Pore formation could be induced through annealing at 300 °C. The average pore area and percentage coverage was controlled by varying the concentration of aspartic acid or glycine in the growth solution, as well as the duration of annealing. The shape of the pores mirrored the morphology of the crystal. It was deduced that the pore formation was the result of a gaseous process involving the evolution of carbon dioxide and water. Possible redistribution of material within the closed pores may occur. This unique pore formation of synthetic calcite occluded with amino acids was compared with geological and biogenic calcite, exhibiting similar trends observed in biominerals, while no pore formation occurred in geological calcite. The results demonstrate a new facile, low cost and low energy methodology to introduce porosity in a controllable manner within single crystals of calcite that may be favourable for diverse applications.

Table of Contents

List of Figures

List of Tables

List of Abbreviations

BUS:	Bottom-up Synthesis
Asp:	Aspartic Acid
Gly:	Glycine
IR	Infrared
TEM	Transmission Electron Microscopy
FESEM	Field Emission Scanning Electron Microscope
TGA/FTIR	Thermogravimetric/Fourier Transform Infrared Spectroscopy
XRD	X-ray Diffraction
THF	Tetrahydrofuran

1 Introduction

1.1 What is Nanotechnology?

Nanotechnology is the control, design and fabrication of material within the range of 1 to 100 nm [1]. There are two approaches to the synthesis of matter on the nanoscale: (i) the top-down approach, in which macroscopic material is reduced to nanoscale dimensions without atomic-level control [2] and (ii) the bottom-up approach, known as "molecular nanotechnology" [1], which involves the engineering of materials from atoms or molecular components through a system of self-assembly.

1.2 Bottom up Synthesis

The potential of bottom-up synthesis (BUS) as a generic scheme of achieving complex material structures of hierarchical assemblies with molecular precision [3], [4] is an alluring prospect. Biological systems employ BUS techniques in order to manufacture structural components (e.g. microtubules formed from α-β tubulin heterodimers [5]) and to impart compartmentalisaton (e.g. vesicles, composed of phospholipids [6]) among others. Biomineralisation refers to the bottom-up synthesis of minerals carried out by organisms [7]. Elements are extracted from the local environment and deposited under strict biological control in order to form functional structures. The materials formed are composites of both organic and inorganic components. Biogenic minerals are found throughout the natural world and exhibit noteworthy properties of which many organisms capitalise upon [8]. The controlled environment under which the biomineral phases are formed results in properties such as crystallinity, shape, size, isotopic and trace element compositions that are very different to the inorganic counterpart [9]. Mineralised structures can fulfill a number of roles, however the most common uses involve feeding, protective, or supportive functions [10].

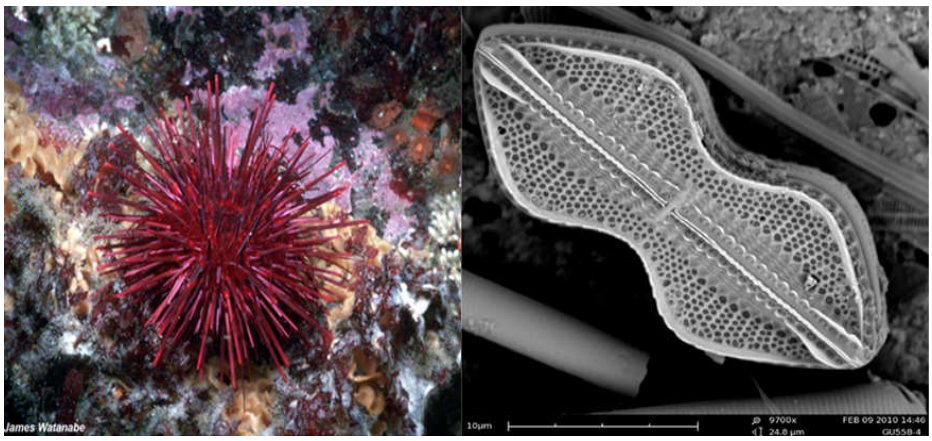

Figure 1-1: Examples of biomineralisation (a) Image of a sea urchin (*Strongylocentrotus franciscanus*) displaying its spines, which are made from a single crystal of biomineralised calcite [11]. The central skeleton is known as the test. (b) An SEM image of a diatom. Diatoms are a major group of algae, characterised by a cell wall biomineralised with silica [12].

Macromolecules produced by the organism direct the growth of the mineral and also contribute to the biomechanical properties of the mature product through the formation of an inorganic/organic composite material [13]. An understanding of the mechanisms by which the macromolecules exert control over nucleation, phase stabilisation, assembly and pattern control of inorganic materials would promote great technological leaps in areas such as the semiconductor industry due to atomistic exactitude [14].

1.3 Calcium Carbonate

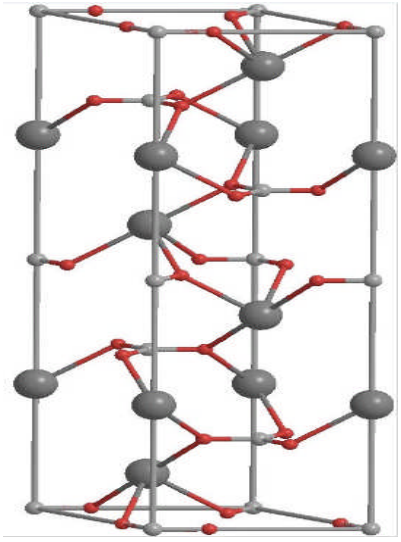

Figure 1-2: Unit cell of calcite [15].

A number of elements have been harnessed for biominerals, however calcium is the most common [16]. Furthermore, in terms of the quantities produced and the widespread

distribution among taxa, calcium carbonate biominerals are the most abundant [7]. More than 4% of the Earth's crust is calcium carbonate and deposits can be found in rocks across the world [17]. Its chemical formula is $CaCO_3$ and it is the main constituent of pearls, eggshells and the shells of marine organisms. Calcium carbonate has industrial applications in areas such as construction, agriculture, plastics, paints, papers, adhesives etc [18].

Anhydrous $CaCO_3$ is a polymorphous compound and occurs in three crystal forms: vaterite, aragonite and calcite [19]. Calcite is the most thermodynamically stable polymorph at ambient conditions and has a rhombohedral prism as the elementary cell of the crystal lattice. A densely packed layer of Ca^{2+} ions are sandwiched between layers of planar carbonate groups (normal to the $\{111\}$ direction), with each successive layer of the anions facing in opposite directions. Each calcium cation is positioned in a distorted octahedral coordination environment, consisting of six carbonate anions [20]. A single calcite crystal is anisotropic, that is, most properties are direction dependent. The crystals are brittle along specific directions known as the cleavage planes. The nonpolar, close-packed array of carbonate and calcium ions results in easy cleavage of the six symmetry equivalent {10.4} crystal faces of the triganol lattice [21], [22]. This is also the cause of the rhombohedral architecture of calcite crystals grown from a supersaturated solution. Cleavage along the low index cleavage planes, (00.1) and (01.2), results in a highly polar crystal face as the cations and anions are separated into different layers, resulting in a dipole moment. Due to the polar nature of these crystal faces, they are not normally expressed in the equilibrium growth form of crystals, however growth in a strongly polar solvent or in the presence of charged inhibitors can lead to their expression [23], [24].

1.4 Biomineralisation

Research into biomineralisation has identified that the hallmark of mineralised skeletal parts is the formation of an amorphous precursor from which a stable single crystal grows [25], [26], [27], [28], [29], [30], [31]. Lowenstam first identified this process in 1962 in his study on the chemical structure of the major lateral denticles in chitons [25], and it has since been found to be widespread in the natural world [27]. Weiner, Sagi and Addadi suggested that this route is taken by organisms because a crystal has a strong proclivity to adopt a specific shape defined by the structure of its crystal lattice, while an amorphous phase can be easily moulded into any shape [27]. Amorphous calcium carbonate (ACC) is an unstable polymorph and efforts to synthesise it in the lab have only been able to do so with one mole of water

per mole of calcium carbonate and under extreme pH or temperature conditions [27]. On the other hand, ACC produced by organisms contains little or no water and is produced at room temperature [28]. The ability to produce single crystals with defined morphologies from an amorphous phase could prove useful for the fabrication of complex-shaped crystalline synthetic materials.

2 Literature Review

2.1 Crystal Nucleation and Growth

Crystallisation processes are involved in a large number of industries including the manufacture of pharmaceuticals, personal care products, agrochemicals, electronics and food to name a few [32]. However, the amount of control over nucleation, growth and orientation that is currently possible through the presence of a controlling matrix or the addition of chemicals that alter crystal growth is minimal [33]. On the contrary, organisms can produce functional, intricate arrangements of crystalline structures and have been for at least the past 750 million years through biomineralisation [34].

A major challenge presented to scientists involved in this area of research is to understand the mechanisms that provide organisms with such a high level of control. There are a number of energy barriers that must be considered when attempting to decipher how crystallisation occurs, and these barriers can be combined into an "energy landscape" to provide an effective model (Figure 2-1).

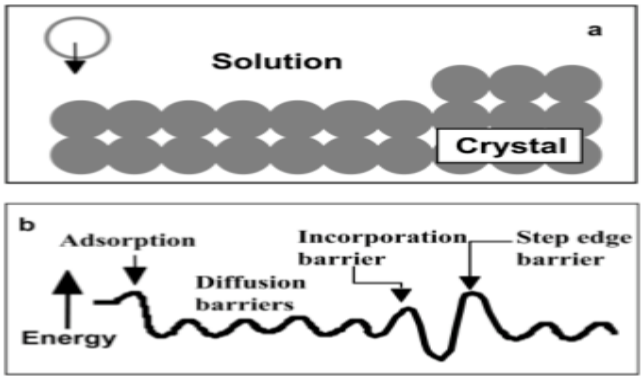

Figure 2-1: Schematic of (a) a solute molecule approaching a physical crystal landscape. (b) the "energy landscape" and the energy barriers that are encountered as a solute particle becomes part of a crystal [35].

Crystallisation involves a phase transition as matter is converted from a state of high free energy in the solvated state to a low free energy state in the crystal lattice. The shape of the energy landscape influences the final properties of the crystal. The depths and shapes of the energy minima determine the crystal phase and habit, while the heights of the energy

barriers alter the growth kinetics and allow intermediate and non-equilibrium final states to be obtained [36]. Organisms can produce complex biomineralised structures through many regulated processes that command this energy landscape.

2.1.1 The Driving Force of Crystallisation

In order for a phase transformation to occur from the solvated state to the solid crystal state, the free energy of the initial solution phase must be greater than the sum of the free energy of the final solution phase plus the free energy of crystalline phase. In other words, the activity product of the reactants, AP, must exceed the equilibrium activity product, K_{sp}, of these reactants [37]. Activity products are often taken as equal to the concentrations of the species that they represent. When the crystallisation involves the phase transformation of a single chemical species, the total free energy change can be expressed as the change in chemical potential of the crystallizing species, $\Delta\mu$. The free energy response to molecules transforming from one phase to another is measured by the value of $\Delta\mu$. The greater the value of $\Delta\mu$, the greater the driving force for crystallisation [38]. The change in chemical potential and the change in free energy are related to the activity products [39]. For the following precipitation reaction (Equation 1)

Equation 1

$$aA + bB + \cdots nN \rightarrow A_a B_b \cdots N_n$$

the value of AP (Equation 2) and K_{sp} (Equation 3) are given by;

Equation 2

$$AP = [A]^a [B]^b [C]^c \cdots [N]^n$$

Equation 3

$$K_{sp} = [A]_e^a [B]_e^b [C]_e^c \cdots [N]_e^n$$

The activity at equilibrium is represented by the subscript 'e'. Using K_{sp}, the Boltzmann constant (k_B) and the absolute temperature (T) the "free energy of solution per molecule" (Δg_{sol}) can be calculated (Equation 4);

Equation 4

$$\Delta g_{sol} = -k_B T \ln K_{sp}$$

Δg_{sol}, AP, the absolute temperature and the Boltzmann constant can be used in conjuntion to calculate $\Delta\mu$ (Equation 5);

Equation 5

$$\Delta\mu = k_B T \ln AP - \Delta g_{sol}$$

Equation 6 demonstrates the relationship between AP, $\Delta\mu$, and K_{sp};

Equation 6

$$\Delta\mu = k_B T \ln(AP / K_{sp})$$

A term that is related to $\Delta\mu$ and often used in crystal growth analyses is the supersaturation, σ. Supersaturation is an essential prerequisite for cystallisation to occur. A solution is supersaturated when the concentration of dissolved solute is above the equilibrium saturation value at a given temperature. Supersaturation is a dimensionless value and can be formally defined as (Equation 7)

Equation 7

$$\sigma = \frac{(\mu_{ss} - \mu_{eq})}{k_B T}$$

in which μ_{ss} represents the chemical potential of a molecule in its supersaturated state and μ_{eq} its equilibrium state. The Gibbs-Duhem equation, an equation that relates the chemical potential to the solute activities can be used to give

Equation 8

$$\sigma = \ln(a_{ss} / a_{eq})$$

wherein a is the activity. In the case of an ideal solution or when the activity coefficient is independent of concentration, this can be reduced to Equation 9

Equation 9

$$\sigma = \ln(\chi_{ss}/\chi_{eq}) \approx (\chi_{ss} - \chi_{eq})/\chi_{eq}$$

where the approximation is valid only at small values of $\chi_{ss} - \chi_{eq}$. For practical reasons, the supersaturation is often expressed in terms of solution concentrations (Equation 10)

Equation 10

$$\Delta c = c_{ss} - c_{eq}$$

in which c has units of molarity.

[35], [40], [41]

Once supersaturation has occurred, crystal nuclei will begin to form. As one can imagine, some of the particles that constitute its make up will be situated at the surface, while some will be in the bulk. The particles at the surface will have a different free energy than those of the bulk because the surface particles do not have their intermolecular interactions fully and homogeneously satisfied. The difference between the free energies is known as the interfacial tension and acts to destabilise the nucleus [38]. The overall excess free energy associated with the process of nucleation in a homogeneous solution (ΔG) can be represented by Equation 11

Equation 11

$$\Delta G = -zk_B T \ln(x_{ss}/x_{eq}) + \beta\gamma z^{2/3}$$

where

- z represents the particles that constitute the crystal nucleus.
- k_B is the Boltzmann constant.
- T is the absolute temperature.
- $\ln(x_{ss}/x_{eq})$ represents the supersaturation as defined by Equation 9.
- β is an area shape factor dependent on nucleus shape.
- γ is the interfacial tension between the developing crystalline surface and the supersaturated solution.

[42]

ΔG is highly dependent upon the number of particles in the nucleus as small bodies have a large surface area/volume ratio. ΔG increases with each addition of a particle and so small nuclei are unstable until a particular nucleus size, known as the critical size, is obtained at which ΔG is at a maximum. At the critical size, the free energy of the system will decrease whether the nucleus destablises or continues to grow and this phenomenon is known as the Gibbs-Thomson effect. The maximum value of ΔG that must be reached until the nucleus is stable acts as an energy barrier. As supersaturation increases, this energy barrier decreases and so does the critical size [43]. The energy barrier can also be decreased through the addition of foreign bodies to the solution, and the extent to which it is lowered is dependent upon how well the "catalysing body" mimics the structure of the crystallising material. In this case, the supersaturation required to induce crystallisation is reduced. This form of nucleation is known as heterogeneous nucleation. The decrease in free energy occurs as a result of an enthalpic contribution. This is due to the formation of interactions that are stronger between the substrate and the nucleus particles, than the bonds of solvation. If specific structural interactions are possible between the crystallising solute and the catalysing body, perhaps as a result of the atomic structure of the substrate closely matching a certain crystal plane or a set of chemical functionalities are presented (stereochemical effect), then the crystal will grow co-aligned with respect to the oriented domains of the substrate [35], [44].

2.1.2 Crystal Growth

The most widely accepted model of crystal growth was proposed by Kossel in 1934 [45] (Figure 2-2). The crystal surface is composed of cubic units. These units form raised partial layers on the crystal surface, known as terraces, themselves limited by steps. The steps contain incomplete regions, known as kinks. When a growth unit attaches at a kink, it forms bonds in three different directions, as opposed to forming one or two on the crystal surface alone or at a step edge, respectively. Therefore, the interactions at a kink site are more favourable and so the growth rates of a crystal, at a given solute concentration, scales with the kink density and thus can be controlled by blocking kinks or roughening steps. As the growth units join on to the crystal at the kink sites, the kink moves along the surface of the crystal until it reaches the edge. Growth then continues by the formation of a new step by the nucleation of a growth unit on the crystal surface. This mechanism is known as layer growth. Another method of growth is the multinucleation multilayer growth mechanism, in

which the nucleation rate of growth units exceeds the time it takes for a step to cover the crystal surface. The nucleated growth units form terraces that spread and then combine to form a layer [35].

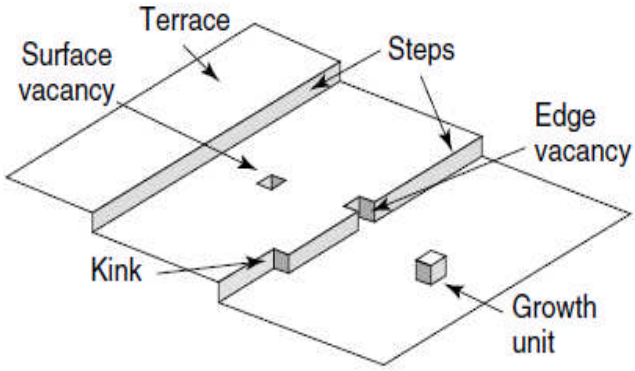

Figure 2-2: Model of crystal growth proposed by Kossel [45].

2.2 Incorporation of Organic Particles into Calcite Crystals

Over forty years ago, Towe and Thompson observed highly concentrated "frothy" structures at crystal boundaries between single crystals of the aragonite nacreous layer of *Mytilus californianus* (Figure 2-3) [46].

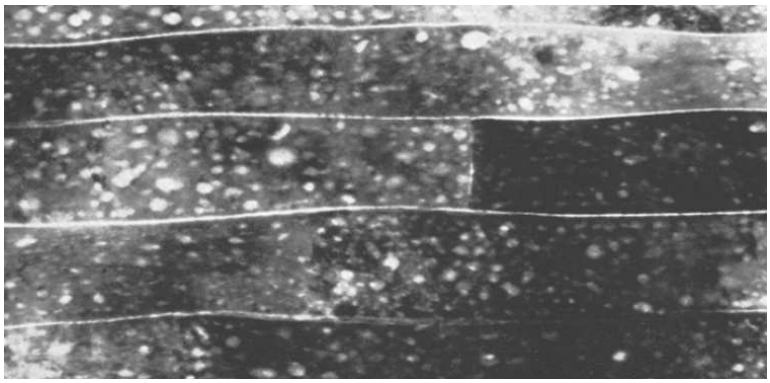

Figure 2-3: TEM image taken by Towe and Thompson in 1972. Each plate represents a single crystal. The boundaries are emphasised by their bright appearance as a result of the loss of organic species and water, leaving behind a fine, frothy structure. The bright spots on the plates indicate that organics and water were also situated within the crystal [46].

These features were studied using transmission electron microscopy and were believed to arise due to the heating effect of the ion-beam sputtering technique used to prepare the samples or from the electron beam in microscopy. No such structures were observed in geological aragonite, and so the morphology was attributed to trapped water and organic material as crystal inclusions [46]. Almost twenty years later, Berman *et al* grew calcite crystals in the presence of fluorescent-labelled sea urchin organic matrix molecules obtained

from the test of *Paracentrotus lividus* [47]. Upon viewing of the crystals in fluorescent light, they were completely illuminated; as were partially dissolved crystals with no remaining original surfaces. This indicated that some of the protein is occluded within the crystal and it was estimated that only about ten protein molecules were present per block of 1 x 10^6 unit cells. The crystals were found to cleave with difficulty, unlike geological calcite. Thus, it was concluded that the low weight percent of occluded protein and the conchoidal nature of the manner in which the crystal fractures indicates that the protein does not form a continuous phase throughout the crystal, but is located at the surface of mosaic blocks within a single crystal (Figure 2-4) [8], [47]. Li *et al,* Sethmann *et al* and Rousseau *et* al have carried out investigations that support this theory [48], [49], [50].

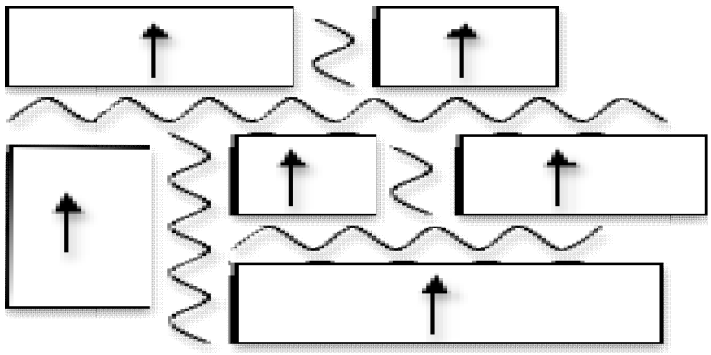

Figure 2-4: Diagram showing the arrangement of inorganic crystal domains and organic macromolecules [51].

"Unusually acidic macromolecules" have been associated with almost every biomineralisation processes [52], [7]. Veis and Perry discovered the first mineralised-tissue acidic macromolecule in 1967 upon the isolation of an acid precipitate fraction from decalcified bovine dentine matrix [53]. This fraction was further separated into two components (the fast (F) and slow (S) components) through electrophoretic studies. The F component was found to be rather unusual after amino acid analyses revealed that aspartic acid (Asp) and serine residues accounted for ~75% of the amino acids present, and it was also particularly rich in phosphate containing residues. Veis and Perry went on to argue that the F component was not merely associated with cellular debris mechanically trapped within the matrix, but instead was an integral part of this structure. The data indicated that component F not only had a proline:hydroxyproline ratio almost identical to the un-degraded dentine matrix, but, significantly, it contained almost all of the hydroxylysine that survived the periodate oxidation; an amino acid that is almost exclusively associated with

collagen [53]. Previous studies [54], [55] had succeeded in removing glycoproteins with similar charge characteristics from the matrix, however extractions with acids, denaturants, concentrated neutral salts and basic solvents had all failed to remove the phosphate containing moieties from dentin [56], supporting the theory that these moieties are intimately associated with the matrix. It has since been proven that the biological growth of carbonate minerals is regulated by macromolecules with an acidic character as a result of an abundance of aspartic and glutamic acid residues [7], [57], [58], [59]. A number of studies have suggested that the acidic macromolecules bind preferentially to specific crystal faces and inhibit growth, thus affecting the overall morphology [47], [59], [60], [61], [62].

When investigating the interactions between acidic proteins and crystals, Addadi and Weiner [60] adsorbed Asp-rich glycoproteins from mollusk shells onto the surface of plastic or glass containers, on which the proteins undertook a β-sheet conformation after binding Ca^{2+}. The orientation resulted in a stereochemical effect that eventuated in a regular array of calcium and carboxylate ions. This promoted the nucleation of calcite from the (001) face to which the carboxylate groups were perpendicularly aligned [60]. This particular orientation, with the c-axis of the calcite crystal aligned perpendicular to the surface of nucleation, is the orientation most commonly found in biological mineralisation [52]. Addadi *et al* noted that poly(aspartic acid) adsorbed onto a substrate is not capable of inducing (001)-oriented calcite nucleation alone, and so suggested that another factor must be involved in producing this orientation. To investigate this, they hypothesised that a local supersaturation of calcium ions is generated by the sulphate groups of the polysaccharides attached to the protein backbone. This encourages the nucleation of calcite on the aligned carboxylate domains. To test this, calcite crystals were grown in the presence of sulphonated polystyrene films with adsorbed poly(aspartate). It was demonstrated that model systems of carboxylate and sulphonate ligands cooperate to stimulate oriented calcite nucleation.

It is now widely accepted that Asp is the most common amino acid responsible for the occlusion of biomacromolecules into calcite [47], [60], [63], [64], [65]. Borukhin *et al* carried out a meticulous study in which they screened the incorporation of all the proteinogenic amino acids into calcite, using Asp as a standard [66]. The concentrations at which the amino acids are incorporated and the effects on the hosting lattice were also investigated. The crystals were grown in solutions of each of the amino acids in turn at 0.5, 2 and 3 mg/ml concentrations at approximately pH7 and the crystals were studied using high-resolution

powder diffraction. They found that as the molar incorporation of the different amino acids increased, as did the induced lattice distortions, although there were specific amino acids that had a relatively stronger or weaker effect than the trend line. Of the acidic amino acids (Asp and Glu), aspartic acid was found in the highest concentrations in the calcite lattice which, due to the overwhelming presence of Asp in biomineralisation-associated macromolecules, is as expected. However, the side chains of these two acidic amino acids only differ by the addition of a single methyl group in Glu. Aizenberg *et al* [67] state that proteins associated with amorphous calcium carbonate are richer in Glu than Asp and that the longer, more flexible side chain of Glu could play a role in disrupting the organisation of the calcite lattice; this could be the cause of lower levels of inclusion found by Borukhin *et al.* Cysteine (Cys) was incorporated surprisingly well and produced large lattice distortions that were disproportionate to the molar ratio in the crystals. The basic amino acids, lysine (Lys), histidine (His) and arginine (Arg), were found to be much lower in concentration within the calcite than the acidic residues, which could be attributed to their basic character. His occurred in the highest molar ratio in the crystals and had the carboxyl terminal group with the lowest pKa. The incorporated concentrations of the basic amino acids were found to correlate to the pKa ratios of the amino and carboxyl terminal groups. Out of the amino acids with hydrophobic side chains, only alanine was present in sufficient concentrations within the crystals so as to be detected by chemical analysis, although XRD detected the remainder of this group. Proline was the only amino acid not detected by either of the analytical techniques. It is plausible that its bulky, inflexible side group confers conformational rigidity resulting in too many local distortions and so preventing it from incorporating. In order to investigate the effect of amino acid size on their incorporation and effect on the crystal structure, the lattice distortion was normalised to the concentration for all of the amino acids. The data revealed that the bulkiness, rigidity and also how well the amino acids can pack together plays an important role in determining the effects of incorporation on lattice distortion. Tryptophan produced the highest normalised distortions, probably due to its rigid structure. Serine, an amino acid that is frequently identified in macromolecules involved in biomineralisation, was found to induce a very small effect on the host lattice. Glycine, the smallest of all the amino acids and commonly found amongst Asp-rich domains of biomineralisation proteins [52], [68], [69], [70], caused relatively large lattice distortions. The authors were unable to provide an explanation for this. Conclusively, the research demonstrated that the ability of an amino acid to incorporate into the crystal

lattice is dependent upon their size, rigidity, polarity, charge and the relative pKa values of the carboxy and amino terminal groups.

The mechanisms by which foreign particles are incorporated into a single crystal have been described [71], [72], [73]. A particle will be occluded if it wets the growth front of the crystal. On the other hand, the particle experiences a repelling “disjoining” force if the wetting is poor, and moves forward with the growth front. Faster growth rates result in an increase in the hydrodynamic force; the force that counteracts the disjoining force[73]. Under a greater hydrodynamic force the particle will be pushed into the crystal and so be incorporated. An increase in the growth rate also increases the transport resistance; as there is less time for molecules and ions to diffuse between the particle and the growth front, further promoting occlusion [71].

2.3 Effect of Organic occlusion on Crystal Properties

A number of groups have investigated the concept of organic molecule occlusion within calcite and the effects on the crystal properties. Kim *et al* investigated the mechanical properties of calcite-polymer particle composites. A simple one-pot synthesis for growing single crystals of calcite in the presence of acidic polystyrene particles was used. A high density of inclusion was achieved and the homogeneous distribution of the particles in solution was maintained within the crystal. Additionally, it was found that the fracture toughness of the calcite was enhanced via a crack bridging mechanism as a result of the polymer particle occlusion. Significantly, this had not previously been observed in a synthetic calcium carbonate system.

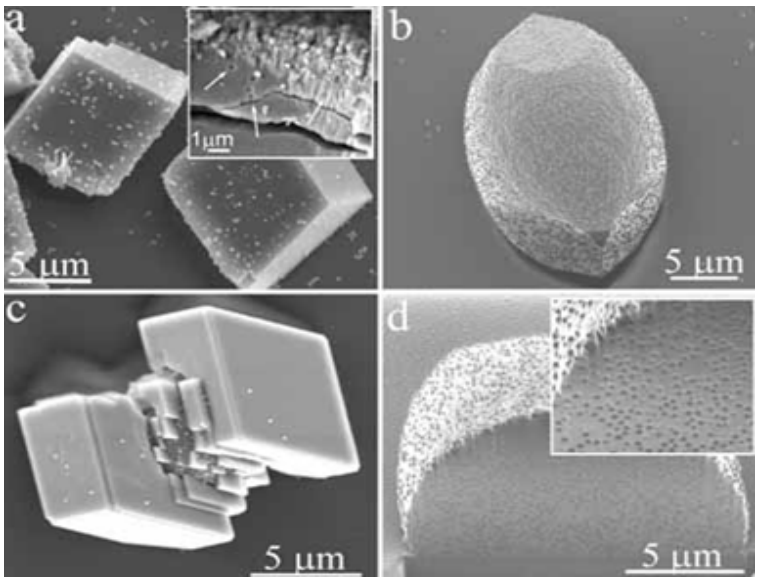

Figure 2-5: Calcite crystals grown by Kim *et al* in the presence of a) [Ca^{2+}] = 1.25 mM, 0.05 wt% carboxylate-functionalised polystyrene particles. The inset contains an image of the cross-section, highlighting that particles are only occluded at the outer surface. (b-d) [Ca^{2+}] = 1.25 mM and 0.05 wt% high acid content polystyrene particles. (b) Morphology of a single crystal. (c) After fresh overgrowth of calcite crystals. (d) cross-section created using FIBS to display the high density of uniformly distributed particles within the crystal [74].

Li and Estroff demonstrated the importance of considering growth kinetics for the incorporation of organic gel networks into calcite, an effect previously only demonstrated for the incorporation of particles [75]. The agarose hydrogel concentration, strength and crystal growth rate were varied in order to examine the factors that determine the amount of incorporation. They proposed that the gel fibres limit mass transport of ions to the growth front, while a crystallisation pressure is exerted on the gel network by the growing crystals. As a result of this competition, they concluded three scenarios may arise: (i) Crystals grown in a weak gel network will not incorporate any material, as the crystallisation pressure will push the network away. (ii) Crystals grown on a strong network with a fast growth rate (high [Ca^{2+}]) will be entirely incorporated. (ii) Partial incorporation will occur if the crystals are grown on a strong network with a slow growth rate.

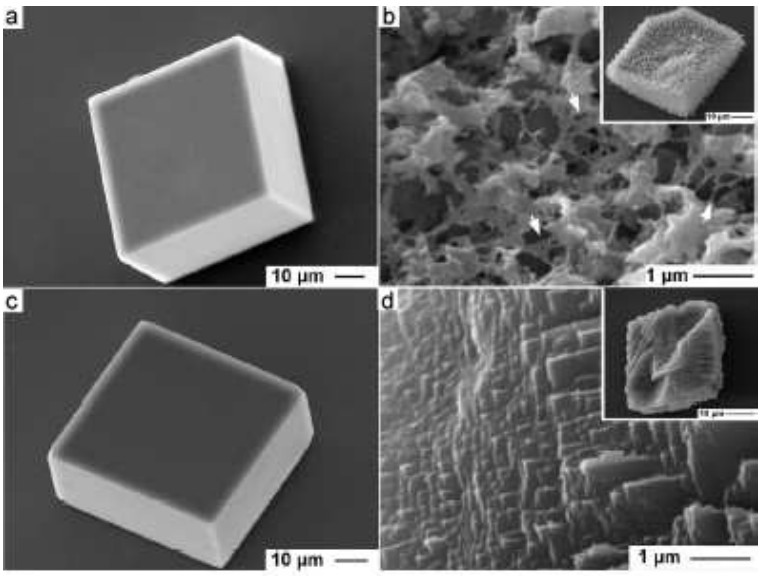

Figure 2-6: Calcite crystals grown in the presence of agarose gel networks by Li and Estroff. (a) Representative SEM image of a calcite crystal grown in an agarose gel (1 w/v% Agarose IB, 5 mM $CaCl_2$) (b) SEM image of a fractured crystal grown under the same conditions as crystal in (a), but etched for four days in deionised water. The white arrows indicate the incorporated gel fibres. (c) Representative SEM image of a calcite crystal grown in a different agaraose gel (1 w/v% Agarose XI, 5 mM $CaCl_2$). (d) fractured crystal grown under the same conditions as in (c), but etched for four days in deionised water [75].

To investigate the level of control copolymers have over crystal morphology or size, Marentette *et al* synthesised calcite in the presence of various ionically polymerised poly(ethylene oxide)-*block*-poly(methacrylic acid) (i.e. PEO-*bl*-PMAA) [76]. The data confirmed a decrease in the growth rate perpendicular to the c-axis, resulting in an elongated shape. It was concluded that the carboxylate groups of the PMAA block specifically adsorbed on planes parallel to the c-axis in a similar orientation to the carbonate ions of $CaCO_3$. The PEO blocks are excluded from the crystallising surface and prevented crystal flocculation through steric hindrance. Also, the relative and absolute lengths of the two blocks of the copolymers were found to be important. It was found that a block ratio of 7.5:1 PEO:PMAA produced the broadest size distribution, while a 1:1 block ratio exhibited a strong inhibiting effect.

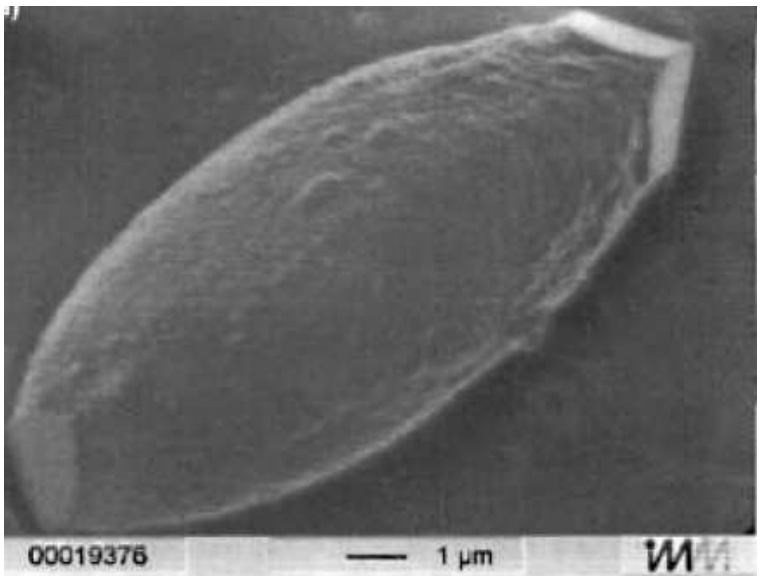

Figure 2-7: An SEM image of the morphology exhibited by the crystals grown in the presence of copolymers by Marentette *et al* [76].

2.4 Formation of Porous Calcite Crystals

The ability to fabricate calcite crystals with pores of defined size and distribution is desirable for applications such as separation technology, biomedical engineering, photonics and catalysis to name a few [77]. The growth of ordered three dimensional porous single crystals has proven challenging, however such intricately structured materials are ubiquitous in nature, for example in the test of sea urchins [78] and the skeletal plates of coccoliths [79]. There have been a number of reports on the formation of porous calcite crystals, a few of which are detailed below.

Kim *et al* grew calcite crystals in the presence of anionic diblock copolymer micelles [80]. The micelles acted as "pseudo-proteins" as their diameter was 20nm and so was within the size range of some naturally occurring intracrystalline proteins. The micelles undertook a disc-like shape on entrapment and a very high level of occlusion was achieved, approximately 20 vol%. The suggested reason for this was that the copolymer micelles, facilitated by the flexible negatively charged carboxylated chains, had a high affinity for the {104} crystal plane and are not displaced by incoming growth units. Furthermore, a uniform size distribution of approximately 10 nm x 32 nm pores was achieved.

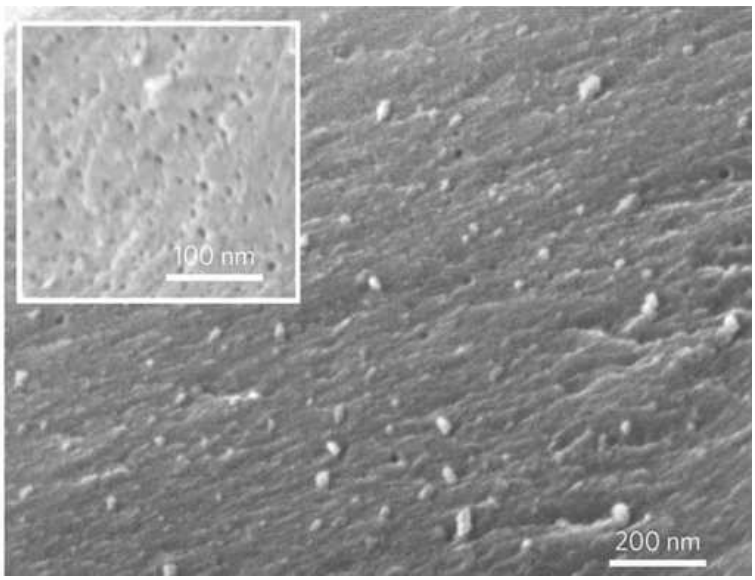

Figure 2-8: An image of a cross-section of a crystal grown by Kim *et al* in the presence of copolymer micelles. The micelles are can be seen as small holes and elongated particles [80].

Lu et al synthesized Rhombohedral calcite crystals with uniform surface pores through templating with colloidal spheres [77]. The monodispersed polymer latex particles, functionalised with carboxylate surface groups, bound to the {104} plane of the crystals. They were densely distributed on the surface layer of the crystal and were only present within the crystals in small quantities. Through further investigation into why the latex particles predominantly occurred at the surface, it was revealed that the particles acted as a substrate for the preferential nucleation of the crystals. As the crystals grew and the calcium ion concentration decreased, the particles attached to the surface layer of the crystals resulting in a uniform distribution. The latex particles could be removed through exposure of the composite crystals to tetrahydrofuran (THF) or calcined at 500 °C. A similar approach was used by Meldum *et al* in which rhombohedral calcite single crystals were grown on monolayers of spherical silica and polystyrene particles, respectively [81]. As a result of the crystals nucleating on the textured substrate, the surface adjacent to the particles reproduced the curvature of the particles but in opposite sign. The topography of the particle array allowed ions to diffuse to the face of the crystal apposed to the surface and so intimate association was achieved. On the other hand, crystals were grown on a PDMS replica of the polystyrene substrate to investigate crystal surfaces with the opposite curvature. The resultant surface associated with the PDMS substrate exhibited hemispheres capped with regular crystal faces. It was concluded that this occurred due to the crystal growth blocking the cavities and so limiting the ion diffusion to the crystal face, resulting in

termination of growth. Li and Qi demonstrated that it is possible to produce highly porous three dimensional ordered macroporous calcite single crystals via a transient amorphous calcium carbonate (ACC) phase [82]. The templating was achieved by infiltration of ACC into 450 nm diameter polymer colloidal crystals with a polystyrene core. These were dried, and then the polymer crystals were removed by dissolving them in THF and calcination at 450 °C. The resultant calcite crystals inherited the hexagonal close packed order of the polymer crystals and displayed a complex network of interconnected spherical voids with diameters of 450 nm throughout. It was proposed that the ACC completely filled the interstices of the polymer crystal template to the top and formed a level imprint patch. A small "tuber" at the centre of this patch preceded oriented nucleation of a core calcite crystal triggering a transformation throughout the calcium carbonate imprint of amorphous to crystalline material. The top (104) face of the growing rhombohedral calcite core was oriented parallel to the top surface of the colloidal crystal. Significantly, this nucleation and growth process resembles the mechanisms observed in nature through which sea urchin larval spicules are formed. These studies, along with many others involving the production of porous calcite through templating [83], [84], [85], [86], [87], [88], demonstrate that the pore size of crystals grown through these methods could be tightly controlled, as the synthesis of templates with predefined dimensions are well established.

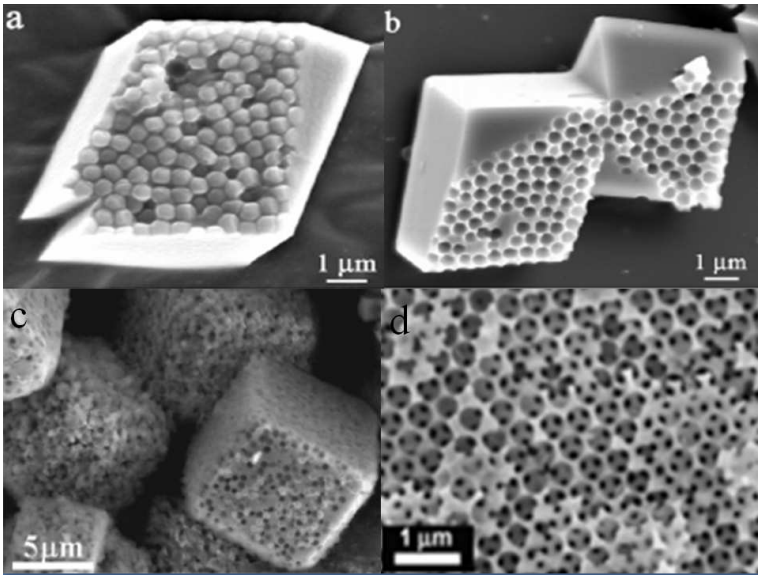

Figure 2-9: (a) Calcite crystal grown by Meldrum *et al* precipitated on a PDMS replica of 0.5 µm particle monolayer. (b) Calcium carbonate crystal precipitated onto 0.5 µm diameter colloidal polystyrene monolayer after dissolution from the spheres [81]. (c) SEM images taken by Lu *et al* of calcite crystals template on monodisperse polymer latex particles of 380 nm diameter [77]. (d) SEM image taken by Li and Qi of a bottom view of the highly porous three dimensional ordered macroporous calcite single crystals they produced [82].

Formation of porous calcium carbonate crystals is dominated by templating strategies; however there are a few reports of alternative methods. One such method, employed by Walsh et al, is through the microwave induced metamorphosis of highly hydrated calcium carbonate hexahydrate (ikaite) crystals with incorporated magnetite [89]. A one-pot synthesis in the presence of carboxymethyldextran (CMD)-coated magnetite nanoparticles at low temperatures (0-4 oC) was used. Magnetite was used due to its excellent microwave absorption properties at frequencies between 0.5 and 10.0 GHz. Upon heating to dryness of the ikaite crystals in the microwave, a crystalline phase transformation to polycrystalline vaterite occurred. These crystals had an open, macroporous and nanotextured structure, with the internal surfaces intimately associated with magnetite nanoparticles. Further, the particles were magnetic and could catalyse water oxidation more effectively than Co_3O_4 nanopowder as a result of their high surface area. Very recently Yu et al also used thermal decomposition to induce porosity in calcium compounds [90]. Approximately 13 mm diameter pellets of calcium carbonate, calcium citrate and calcium lactobionate were heated to 1000 ^{o}C for 60 mins. This caused decomposition to CaO, and cooling yielded porous calcium carbonate products with pores of approximately 100 nm, 1 µm and 20-90 µm respectively. It was proposed that the difference in pore size between the samples was caused by the larger organic molecules leaving more empty space as they depart from the crystal. Also, calcium lactobionate powder was mixed with calcium carbonate powder and compressed into pellets of different molar ratios. Subsequently, the greater the molar ratio of calcium lactobionate, the larger the pores would be in the heat treated product.

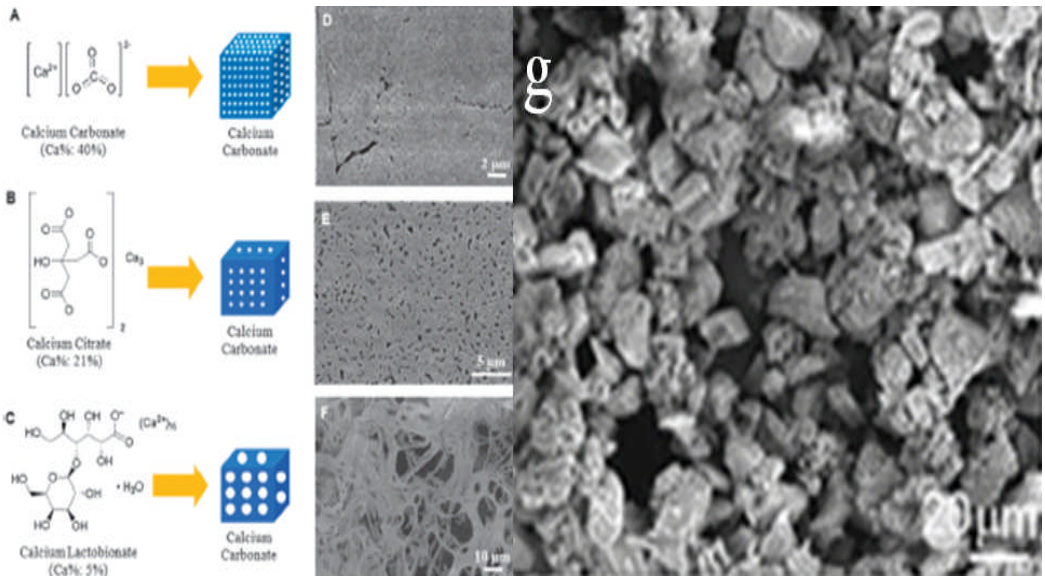

Figure 2-10: (a-f) Crystals synthesized by Yu *et al*. (a) Calcium carbonate (Ca wt% of 40%). (b) Calcium citrate (Ca wt% of 21%). (c) Calcium lactobionate (Ca wt% of 5%). (d-f) Corresponding porous products after thermal treatment at 1000 °C for 60 mins [90]. (g) SEM micrograph taken by Walsh *et al* of highly porous calcite formed by microwave heating prepared ikaite crystals with incorporated magnetite [89].

3 Aims and Objectives

The significance of this report lies in the fact that the majority of research into the interactions of biological molecules with biomineralisation processes is concerned with macromolecules, principally proteins. Very little research has gone into the interactions of individual amino acids with crystalline structures. Additionally, the majority of pore formation in inorganic materials involves templating processes, which can be tedious procedures with regards to separating the crystal from the template, usually mechanically or by dissolving the template in a solvent or by calcination. If dissolving or calcination methods are employed, material waste is inherent. This report examines a facile mechanism by which porosity occurs in calcite single crystals with organic occlusions; a system that, if understood, could be applied to other inorganic/organic composites.

The general aims of this experimental research project are to:

- Investigate the unknown mechanism of internal pore formation upon annealing in calcite single crystals with occluded aspartic acid and glycine and compare with geological and biogenic calcites.
- To determine the evolved species on pore formation.

- To determine the mechanism of pore formation.

The specific objectives of this research project are:

- To synthesise calcite crystals using the ammonia diffusion method.
- To characterize the calcite crystals using optical microscopy, infrared spectroscopy and Raman microscopy.
- To quantify the pores formed within the calcite crystals using a combination of Scanning Electron Microscopy and Image J Analysis software.
- To determine the mechanism of pore formation through the use of;
  - Simultaneous recording of signals from Thermogravimetric Analysis/Fourier Transform Infrared Spectrometry.
  - In situ observation using a Transmission Electron Microscope with Thermal Stage.

4 Experimental

In this section the techniques employed to synthesise and characterize the biomineralised calcite crystals are discussed. The method of inducing pore formation and the procedures used to investigate them are also considered.

4.1 Biomimetic Synthesis of Calcite Single Crystals

Calcium carbonate was precipitated using the ammonia diffusion technique. The use of this method to synthesise calcium carbonate is supported throughout the literature [66], [91], [92], [93].

Glass microscope slides were cleaned and etched by immersion in piranha solution (75 vol% H_2SO_4, 25 vol% H_2O_2). These were then placed in plastic petri dishes to act as substrates for precipitation. They were then submerged in the respective concentrations of reactant solutions containing calcium chloride ($CaCl_2$) and L-aspartic acid sodium salt monohydrate ($C_4H_6NO_4Na.H_2O$) (Table 1).

Sample	*[Asp] (mMol)*	*[Gly] (mMol)*	*[Ca^{2+}] (mMol)*
P3A	5	-	10
P3B	20	-	10
P3C	50	-	10
P3D	20	-	1
P3X	-	5	10
P3Y	-	20	10
P3Z	-	50	10

Table 1: Concentrations of Reactant Solutions

These were covered with parafilm (pierced with six needle holes) and placed in a sealed dessicator with two petri dishes, each containing 2g of crushed ammonium carbonate and also sealed with parafilm (pierced with 6 needle holes). After a crystallisation time of 24h, these were then removed and the slides were washed with distilled water and dried with ethanol.

4.2 Characterisation of Calcite Crystals

In order to ensure that calcite crystals were present and to characterise their morphology, a variety of techniques were used.

4.2.1 Optical Microscopy/Low Resolution Scanning Electron Microscopy

The biomineralised calcite crystals were characterised via bright field microscopy using a Nikon Eclipse LV100. The crystals were viewed on the glass slides that they had grown on.

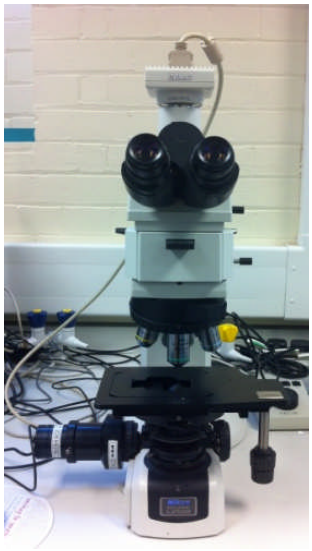

Figure 4-1: Nikon Eclipse LV100 Optical Microscope

4.2.2 Infrared Spectroscopy

Each of the samples were analysed using a Perkin Elmer Spectrum 100 FTIR spectrometer (Figure 4-2). The spectra were taken using a 4000 – 600 cm^{-1} range. IR spectroscopy exploits the correlation between the vibrational transition energy of a specific bond and the frequency of the absorbed radiation. IR spectroscopy is a bulk analytical technique and can be used to distinguish polymorphs, their purity and identify the chemical compounds present and their structure [94]. Absorption peaks in the range of 712-714 cm^{-1}, 868-876 cm^{-1} and 1395-1420 cm^{-1} are expected for calcite.

Figure 4-2: (left) Perkin Elmer Spectrum 100 FTIR Spectrometer, (right) Renishaw inVIa Raman Microscope

4.2.3 Raman Microscopy

To compliment the spectra taken using IR spectroscopy, Raman spectra were taken in a 1200 – 100 cm^{-1} range using a Renishaw inVia Raman Microscope (Figure 4-2). A laser is fired at an individual selected using the microscope and so the Raman spectrum represents a single crystal. The photons of the laser are scattered by molecules within the crystal and as a result the energy of the irradiating photon is altered. The change in energy is characteristic to particular bonds within the molecule and so a spectral fingerprint can be generated of a molecular structure. This technique can provide data on the polymorphic form of the crystal, intrinsic stress and its orientation and purity [95]. To confirm the presence of calcite, signals should be evident at 281, 711 and 1085 cm^{-1}.

4.3 Pore Formation and Characterisation

Pore formation was induced using a Nabertherm P300 annealing oven and a FiStreem vacuum oven (Figure 4-3). The temperatures and exposure times are detailed in Table 2. All of the synthesized crystals were exposed to each of the temperatures for the corresponding durations. The group name was then added to the end of the sample name for identification (i.e. P3AH was 5mM [Asp], 10mM [Ca^{2+}] and exposed to 300 °C for 30mins etc). A heating rate of 10 °C min^{-1} was used for all heating programmes.

Group Name	***Temperature (°C)***	***Exposure Time (mins)***
H	300	30
I	300	120

J	300	720
K	200	30
L	200	120
M	200	720
F	140	30
W	170	120

Table 2: Table detailing the temperature and exposure times of the different groups of calcite crystals

Figure 4-3: (left) Nabertherm P300 annealling overn, (right) FiStreem Vacuum oven

4.3.1 High-resolution Field Emission Scanning electron microscopy (FESEM)

After the annealing procedure, the crystals were broken open using mechanical force and coated in a Pt/Pd alloy. The pores on the interior of the crystals were observed using a Zeiss Leo 1530 Gemini SEM (Figure 4-4).

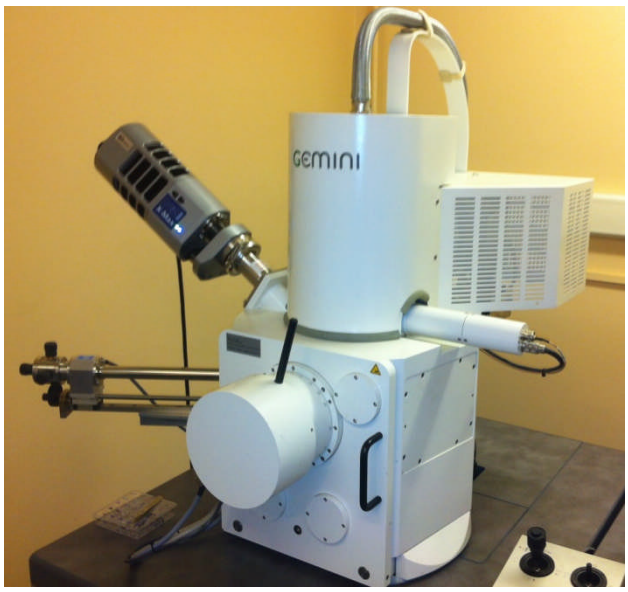

Figure 4-4: Zeiss Leo 1530 Gemini SEM

4.3.2 Image J

Image J is a public domain image processing and analysis software developed at the National Institutes of Health. SEM images of the pores were loaded into the software, prepared for analysis through optimisation of contrast/brightness and then the pore analyses were carried out.

4.3.3 Transmission Electron Microscopy/Thermal Stage

Using a CM200 TEM/Gatan Single Tilt Heating Stage (Figure 4-5) it was possible to qualitatively assess the *in situ* dynamics of pore formation. The mechanically broken samples were mounted on a 75 nm thick silicon nitride grid with a 140 μm window, observed at 200 keV and micrographs were taken every 10 °C from room temperature to approximately 400 °C. To avoid beam damage of the samples, all samples were carefully examined under low magnification.

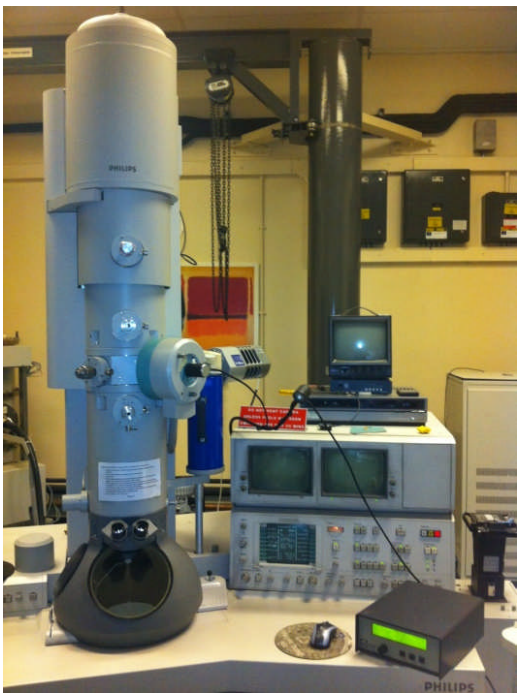

Figure 4-5: CM200 TEM/Gatan Single Tilt Heating Stage

4.3.4 Thermogravimetric Analysis (TGA)/Fourier Transmission Infrared Spectroscopy (FTIR)

Powdered crystals were placed in a Stanton Red Croft TGH 1000 (TGA) linked to a Thermo IS10 (FTIR spectrometer) and heated from room temperature (25 °C) to 600 °C with a heating rate of 10 °C/s. Spectra were taken through the mid infrared region (4000 – 400 cm^{-1}). TGA is a quantitative thermal analytical technique in which a sample is exposed to a controlled heating programme and the change in mass relative to the temperature is recorded. When coupled with Fourier transmission infrared spectroscopy, it is possible to determine the species of the gases evolved during the heating process.

4.3.5 Surface Area and Density Measurement

In order to measure the surface area of a calcite crystal grown in 50 mM Asp (P3C) and annealed at 300 °C for 120 mins a BET surface area analysis was carried out using nitrogen gas. Geological calcite was also measured to provide a comparison.

5 Results

5.1 Characterisation of Calcite Crystals

Optical Micrographs of each sample were taken at 100x and 500x magnification, respectively.

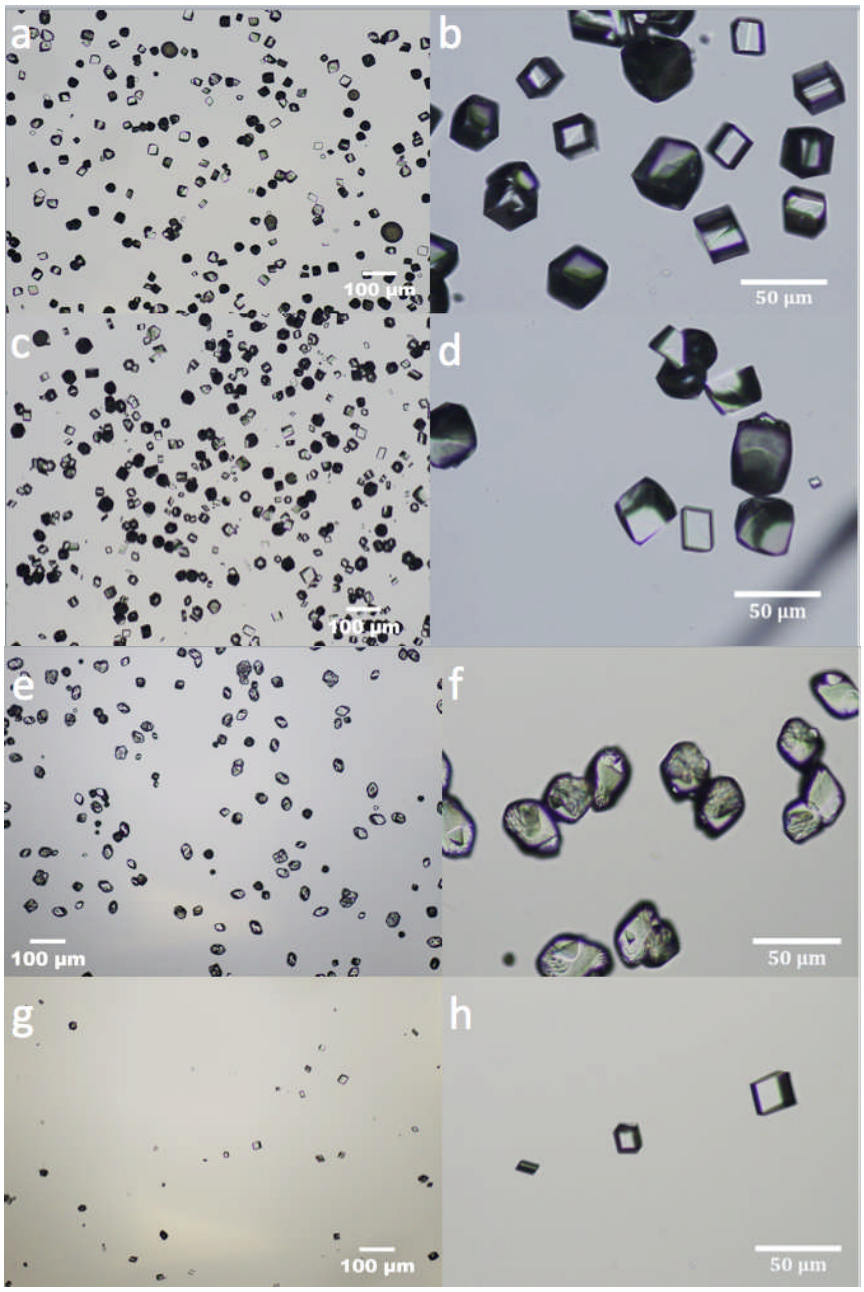

Figure 5-1: Optical microscope images of calcite crystals precipitated in the presence of aspartic acid at fixed Ca 10 mM (a)-(e). (a) P3A, 5mM Asp, at 100x magnification (b) P3A, 5mM Asp, at 500x magnification (c) P3B, 20mM Asp, at 100x magnification (d) P3B, 20mM

Asp, at 500x magnification (e) P3C, 50 mM Asp, at 100x magnification (e) P3C, 50 mM Asp, at 500x magnification (f) P3D, 20 mM Asp, 1 mM Ca^{2+}, at 100x magnification (g) P3D, 20 mM Asp, 1 mM Ca^{2+}, at 500x magnification.

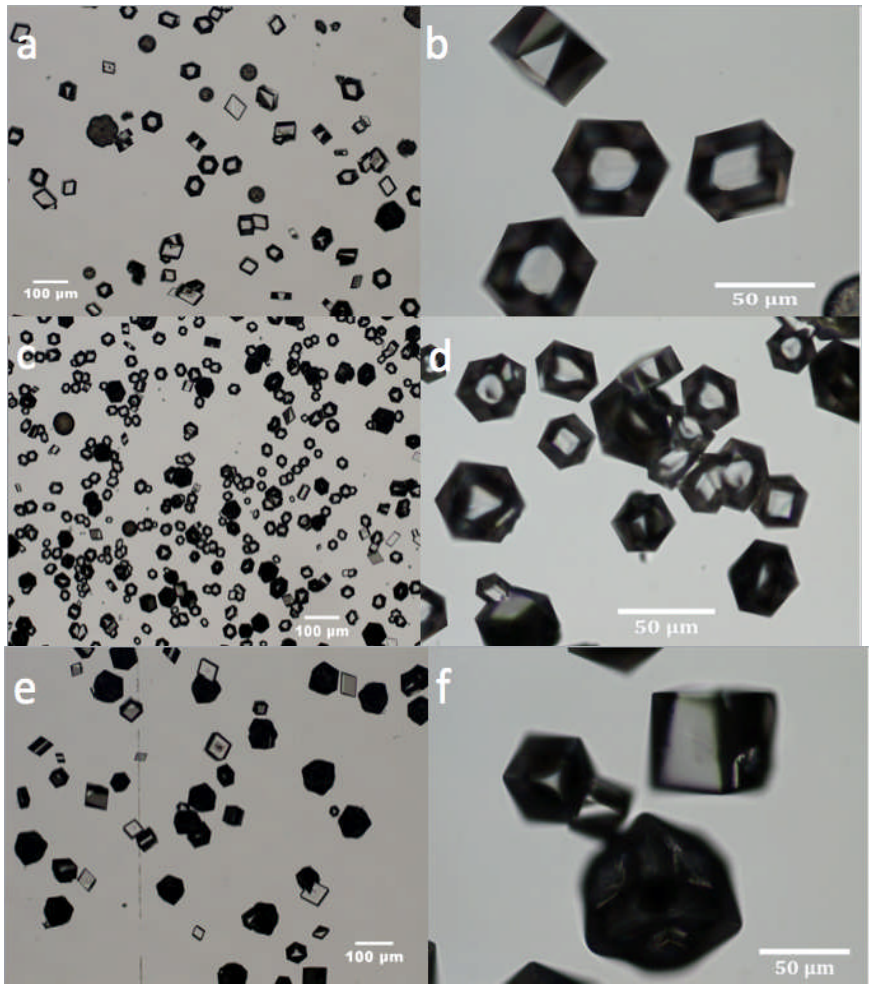

Figure 5-2: Optical microscope images of calcite crystals precipitated in the presence of glycine at fixed Ca 10 mM. (a) P3X, 5mM Gly, at 100x magnification (b) P3X, 5mM Gly, at 500x magnification (c) P3Y, 20mM Gly, at 100x magnification (d) P3Y, 20mM Asp, at 500x magnification (e) P3Z, 50 mM Gly, at 100x magnification (e) P3Z, 50 mM Gly, at 500x magnification.

It is clear from the optical micrographs, that as the concentration of Asp increases, the shape of the crystals tends towards a 'rugby ball' shape. The crystals grown in 5 mM (P3A) and 20 mM (P3B) Asp exhibit slight truncation compared to the expected rhombohedral shape of pure calcite, while the crystals grown in 50 mM (P3C) Asp bear no resemblance to pure calcite crystals at all. Crystals grown in 20 mM Asp and 1 mM Ca^{2+} maintained the rhombohedral form of pure calcite. On the other hand the calcite crystals grown in glycine only exhibit minor truncation at 50 mM (P3Z) Gly concentrations; at 5 mM (P3X) and 20 mM (P3Y) the rhombohedral form is conserved.

Compared to the micrographs of the other samples, P3D displays a much lower density of crystals. The variation in density between the remaining micrographs shall not be considered as they represent small regions of the whole sample, and in actual fact the density of crystals between these samples (all grown in 10 mM Ca^{2+}) was quite similar.

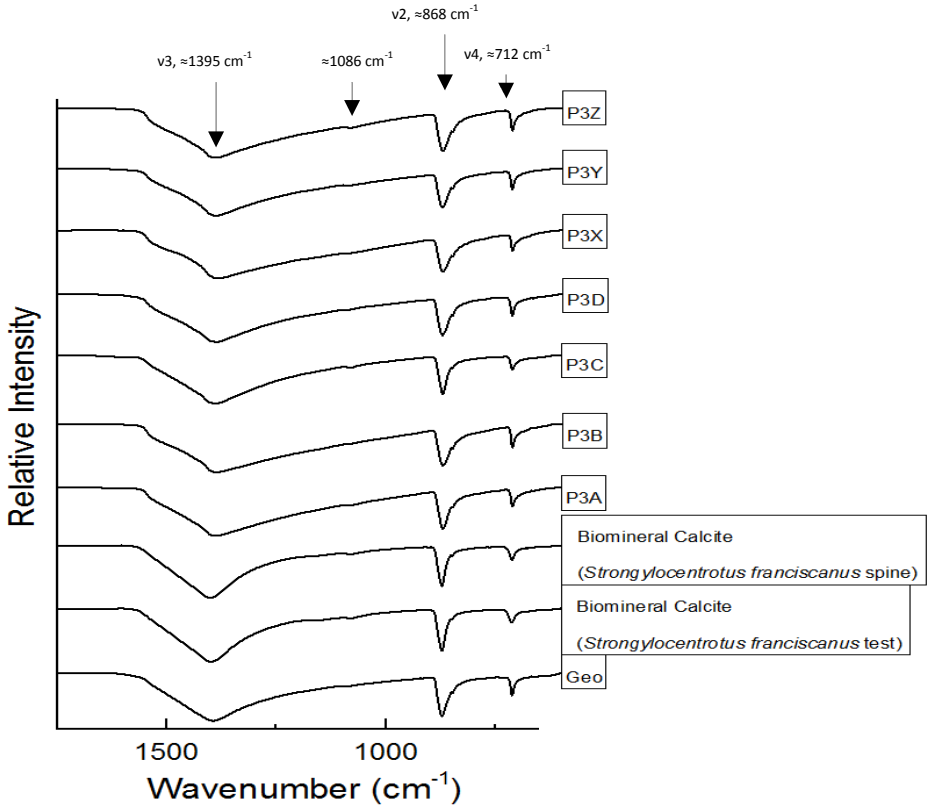

Figure 5-3: IR spectra for all samples including geological and biomineral calcite. Each spectrum shows a peak at approx. 1395 cm^{-1} (v3), 868 cm^{-1} (v2) and 712 cm^{-1} (v4), which are characteristic of calcite. The biomineralised samples also exhibit a peak at 1086 cm^{-1}.

Sample Name and Conditions	ν_2/ν_4
P3A (5 mM Asp, 10 mM Ca^{2+})	2.126
P3B (20 mM Asp, 10 mM Ca^{2+})	1.713
P3C (50 mM Asp, 10 mM Ca^{2+})	3.52
P3D(20 mM Asp, 1 mM Ca^{2+})	1.916
P3X (5 mM Gly, 10 mM Ca^{2+})	2.532
P3Y (20 mM Gly, 10 mM Ca^{2+})	1.808
P3Z (50 mM Gly, 10 mM Ca^{2+})	1.814
Geological Calcite	2.458
Sea Urchin Spine (*Strongylocentrotus franciscanus*)	2.901
Sea Urchin Test (*Strongylocentrotus franciscanus*)	3.086

Table 3: Table of v2/ v4 ratios of all samples including geological and biomineral calcite.

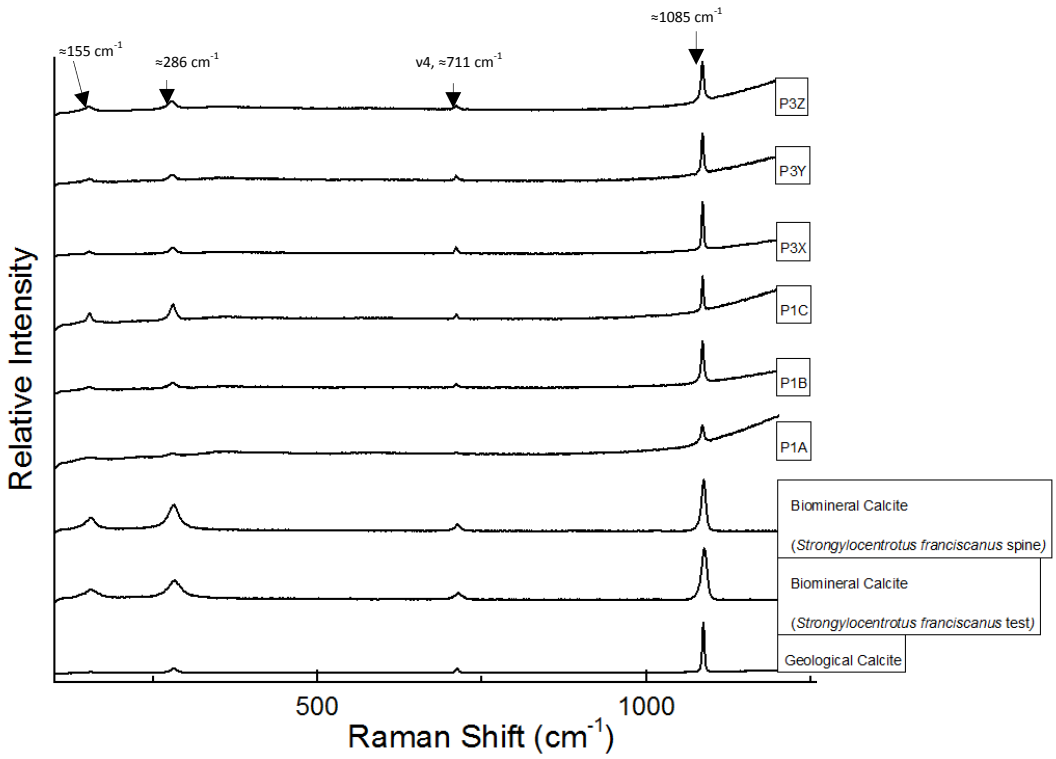

Figure 5-4: Raman Spectra for all samples including geological and biomineral calcite. Each spectrum exhibits a peak at 155, 286, 711 and 1085 cm^{-1}.

All samples were also characterized with IR spectroscopy to identify the polymorphs and internal structure of samples. All samples were calcite, with minor phase of vaterite, especially when higher concentrations of Asp or Gly were used.

The ratio of v2/v4 was also calculated to elucidate the change of internal structure depending on the amino acid concentration.

The IR and Raman spectra complement each other in confirming the presence of calcite. The Raman spectra display a peak at 1085 cm^{-1} and 716 cm^{-1} (v4), this corresponds to the internal CO_3^{2-} symmetric stretch and symmetric bending modes, respectively. The lattice mode peaks are at 155 and 286 cm^{-1}. The IR spectra of the synthetic samples show a slight peak at 1086 cm^{-1}, which is most prominent in P3C and P3Z and not active in the geological sample. This peak corresponds to the occluded organic material and its more distinct nature in samples P3C and Z is representative of the higher concentrations of amino acids present in the sample. The ratio between the peak intensity of v_2/v_4 from the IR spectrum of the sample gives an indication of the atomic order of the calcite crystals. For amorphous calcium carbonate, a value of 10 is expected and for calcite, a value of 3. The values obtained for each sample are all in correspondence with the presence of calcite, however no correlation between amino acid concentration and v_2/v_4 ratio can be identified.

5.2 Formation of Pores in Calcite Crystals

5.2.1 Qualitative Assessment of Pores using Scanning Electron Microscope Micrographs

Shown here are images of the crystals after exposure to the aforementioned temperatures and times. An image from each group was taken that best represents the collective.

Each sample of crystals exposed to 200 °C for 720 mins failed to form pores, while all the samples formed pores after 30 mins at 300 °C. As a result of this, the sample groups annealed at 200 °C for 30 mins and 120 mins were not investigated, as it is unlikely that pores would form when exposed to this temperature at shorter timescales. The fact that pores did not form at 200 °C indicates that somewhere between 200 °C and 300 °C there is a thermal threshold, at which the temperature is sufficient to induce pore formation. Upon observation of sample P3C in the TEM, it was noticed that pores formed at a lower temperature; approximately 140 °C. It was hypothesised that this was due to the vacuous environment inside the TEM, and so to test this, a sample was placed in the vacuum oven at 140 °C for 30 mins (F) and 170 °C for 120 mins (W). High-res SEM revealed that no pores were present in P3CF, whereas a small number of pores could be seen in P3CW. This

indicated that the mechanism by which the pores form involves a gaseous process, as the reduced pressure allows the gases involved in the formation of pores to evolve at a lower temperature.

The electron micrographs reveal that as the concentration of Asp increases, the shape of the pores progress from a rhombus shape at 5 mM to a circular/oval shape at 50 mM, regardless of the duration of exposure to 300 °C. However, longer exposure times and higher [Asp] results in larger pores and a greater density. On the contrary, a change in pore shape with increasing [Gly] is not noticeable, but the density of pores and their size does increase with [Gly] and exposure time.

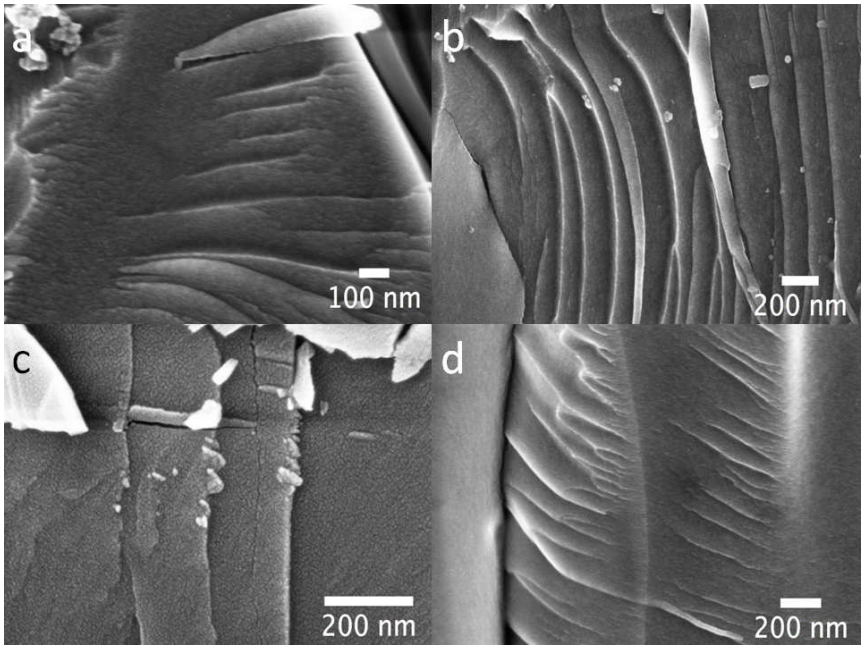

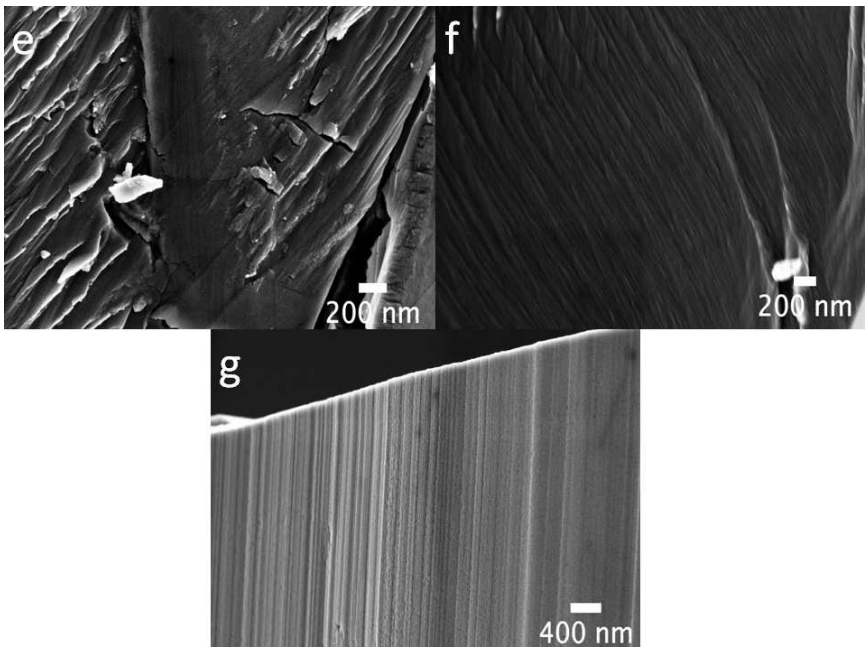

Figure: 5-5 M group (200 ^{o}C, 720 mins). (a) 5 mM Asp (P3A), (b) 20 mM Asp (P3B), (c) 50 mM Asp (P3C), (d) 20 mM Asp, 1 mM Ca^{2+} (P3D), (e) 5 mM Gly (P3X), (f) 20 mM Gly (P3Y), (g) 50 mM Gly.

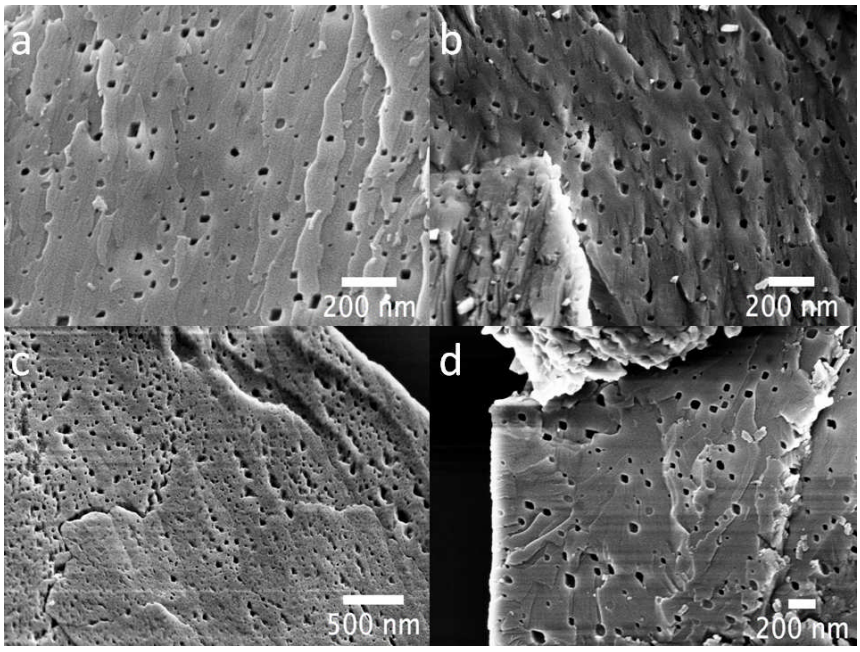

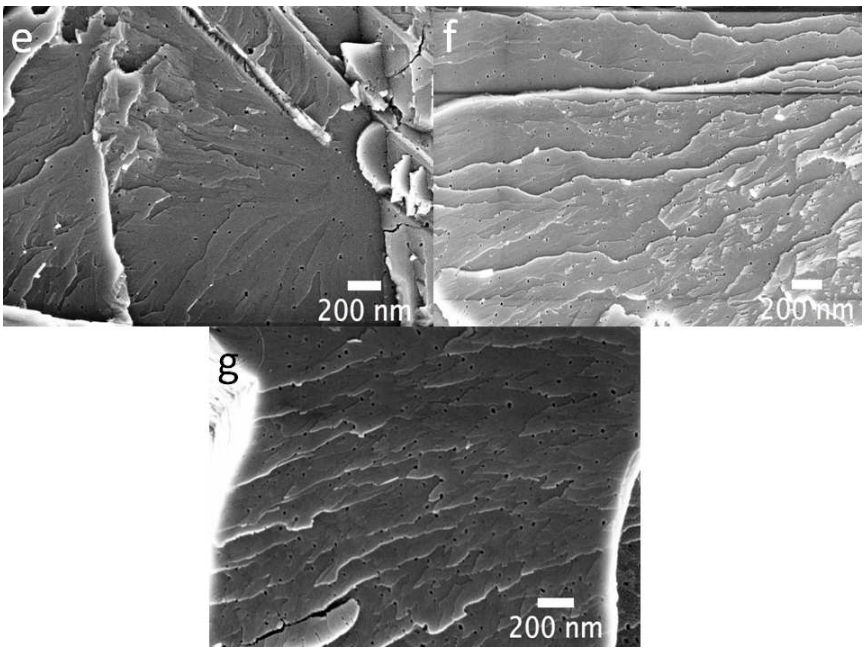

Figure 5-6: H group (300 ^{o}C, 30 mins). (a) 5 mM Asp (P3A), (b) 20 mM Asp (P3B), (c) 50 mM Asp (P3C), (d) 20 mM Asp, 1 mM Ca^{2+} (P3D), (e) 5 mM Gly (P3X), (f) 20 mM Gly (P3Y), (g) 50 mM Gly.

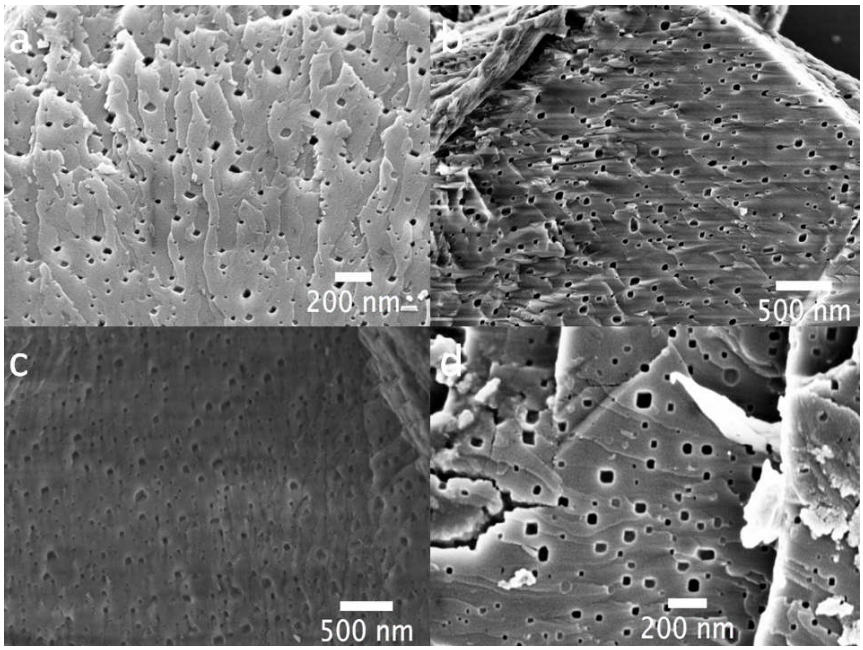

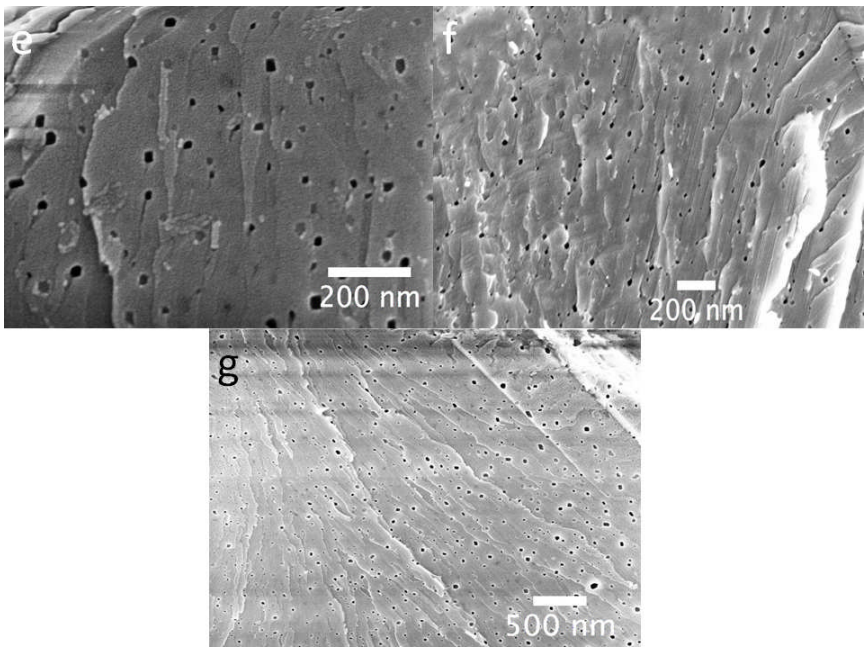

Figure 5-7: I group (300 ^{o}C, 120 mins). (a) 5 mM Asp (P3A), (b) 20 mM Asp (P3B), (c) 50 mM Asp (P3C), (d) 20 mM Asp, 1 mM Ca^{2+} (P3D), (e) 5 mM Gly (P3X), (f) 20 mM Gly (P3Y), (g) 50 mM Gly.

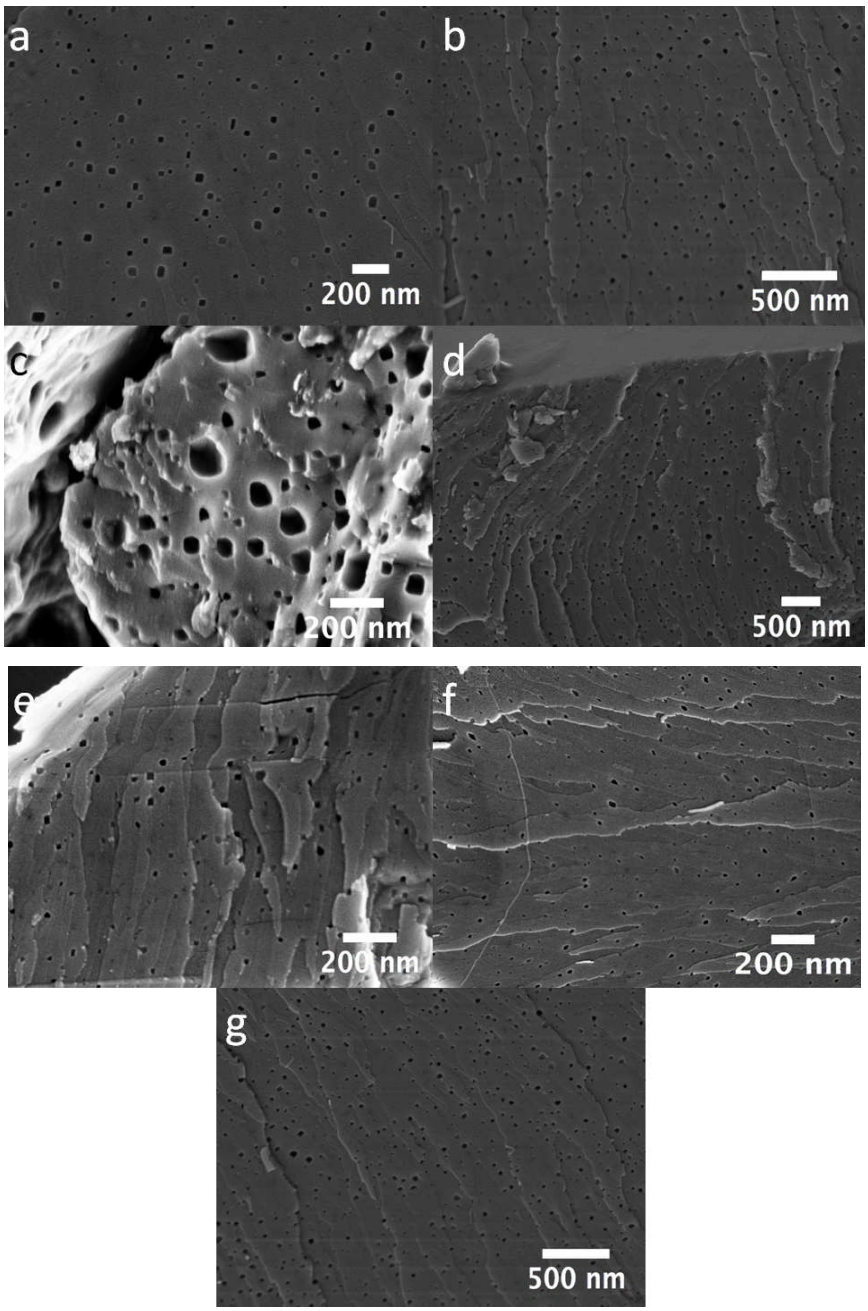

Figure 5-8: I group (300 ^{o}C, 720 mins). (a) 5 mM Asp (P3A), (b) 20 mM Asp (P3B), (c) 50 mM Asp (P3C), (d) 20 mM Asp, 1 mM Ca^{2+} (P3D), (e) 5 mM Gly (P3X), (f) 20 mM Gly (P3Y), (g) 50 mM Gly.

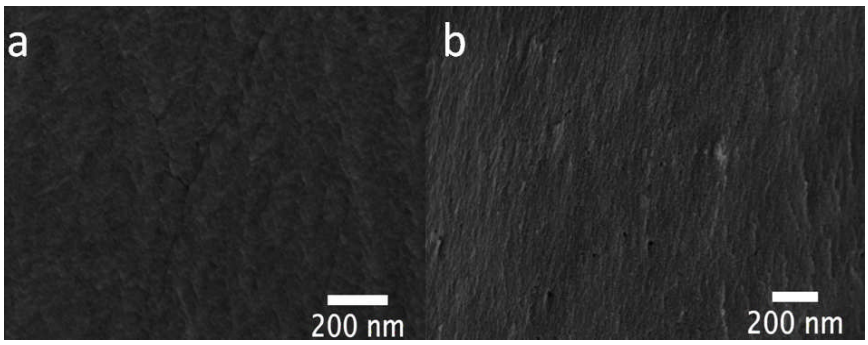

Figure 5-9: (a) Sample P3CF, 50 mM Asp exposed to 140 °C for 30 mins, (b) Sample P3CW, 50 mM Asp exposed to 170 °C for 120 mins.

5.2.2 Quantitative Assessment of Pores using Image J software

The average pore area and percentage coverage were obtained using the "analyze particles" function of the Image J analysis software. The average individual pore area is defined as the sum of the area of each single pore divided by the total number of pores. The percentage coverage is the sum of the area of each single pore divided by the total area of the image multiplied by 100.

	Sample Name	***Average individual pore area (nm^2)***	***% coverage***
1	P3AH (5 mM Asp, 10 mM Ca^{2+}. 300 °C, 30 mins)	489.131	2.698
2	P3BH (20 mM Asp, 10 mM Ca^{2+}. 300 °C, 30 mins)	691.499	3.838
3	P3CH (50 mM Asp, 10 mM Ca^{2+}. 300 °C, 30 mins)	888.386	9.049
4	P3DH (20 mM Asp, 1 mM Ca^{2+}. 300 °C, 30 mins)	949.413	3.660
5	P3AI (5 mM Asp, 10 mM Ca^{2+}. 300 °C, 120 mins)	549.020	3.856

6	P3BI (20 mM Asp, 10 mM Ca^{2+}. 300 °C, 120 mins)	929.357	5.585
7	P3CI (50 mM Asp, 10 mM Ca^{2+}. 300 °C, 120 mins)	1108.647	9.419
8	P3DI (20 mM Asp, 1 mM Ca^{2+}. 300 °C, 120 mins)	1188.661	5.816
9	P3AJ (5 mM Asp, 10 mM Ca^{2+}. 300 °C, 720 mins)	747.502	5.063
10	P3BJ (20 mM Asp, 10 mM Ca^{2+}. 300 °C, 720 mins)	1016.122	7.477
11	P3CJ (50 mM Asp, 10 mM Ca^{2+}. 300 °C, 720 mins)	1190.551	10.583
12	P3DJ (20 mM Asp, 1 mM Ca^{2+}. 300 °C, 720 mins)	1200.191	5.942
13	P3XH (5 mM Gly, 10 mM Ca^{2+}. 300 °C, 30 mins)	320.518	0.746

14	P3YH (20 mM Gly, 10 mM Ca^{2+}. 300 °C, 30 mins)	382.683	1.578
15	P3ZH (50 mM Gly, 10 mM Ca^{2+}. 300 °C, 30 mins)	522.516	2.557
16	P3XI (5 mM Gly, 10 mM Ca^{2+}. 300 °C, 120 mins)	441.803	1.945
17	P3YI (20 mM Gly, 10 mM Ca^{2+}. 300 °C, 120 mins)	603.788	3.249
18	P3ZI (50 mM Gly, 10 mM Ca^{2+}. 300 °C, 120 mins)	823.399	5.067
19	P3XJ (5 mM Gly, 10 mM Ca^{2+}. 300 °C, 720 mins)	452.968	4.287
20	P3YJ (20 mM Gly, 10 mM Ca^{2+}. 300 °C, 720 mins)	628.748	4.433
21	P3ZJ (50 mM Gly, 10 mM Ca^{2+}. 300 °C, 720 mins)	874.004	5.291

Table 4: Mean average values obtained for the average individual pore area and the percentage coverage.

5.2.2.1 Effect of Concentration of Amino Acids (Aspartic acid and Glycine) on Pore Formation

5.2.2.1.1 Aspartic Acid

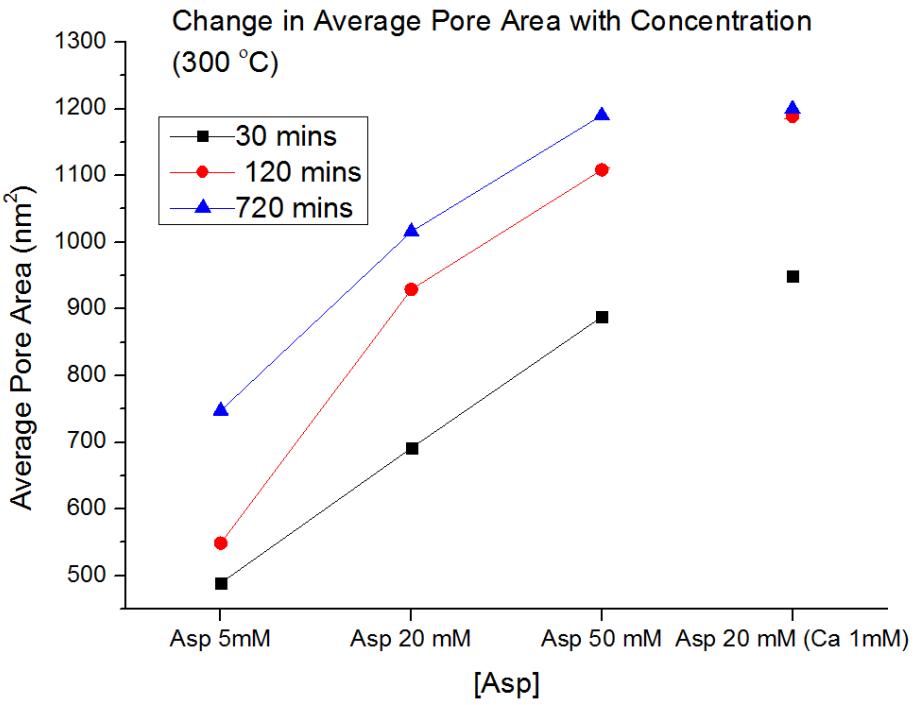

Figure 5-10: Change in pore area with concentration for calcite crystals grown in the presence of aspartic acid

An increase in pore area was observed with increasing concentration of Asp between samples grown in solutions of 10 mM Ca^{2+}. Contrary to what would be expected, the crystals grown in 20 mM Asp and 1 mM Ca^{2+} displayed the largest pore areas, with values comparable to crystals grown in 50 mM Asp and 10 mM Ca^{2+}. The graph also demonstrates how the largest change in pore area occurs between exposure times of 30 mins and 120 mins (with the exception of Asp 5 mM).

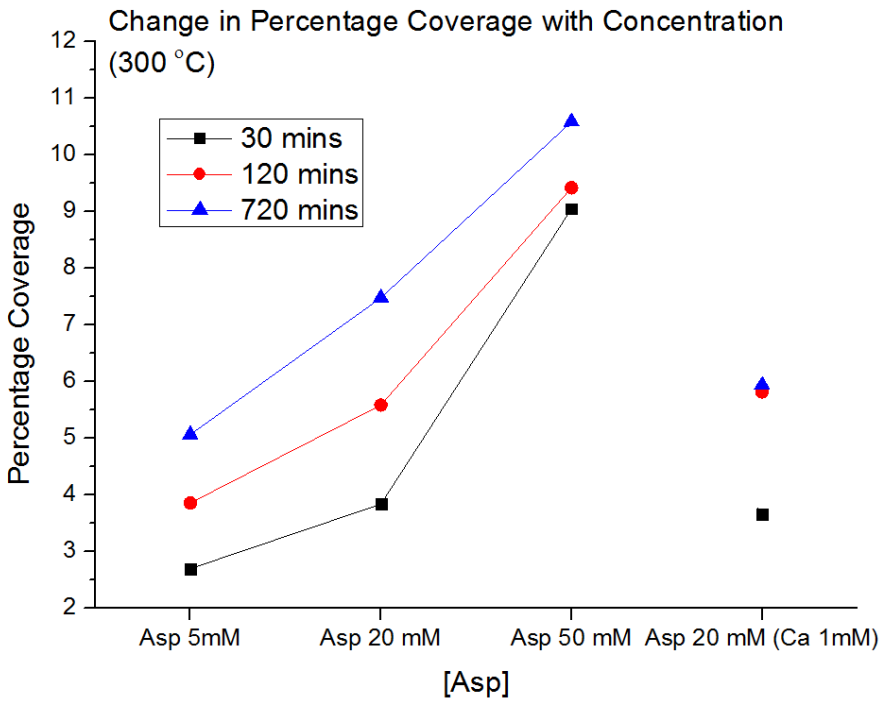

Figure 5-11: Change in percentage coverage with concentration for calcite crystals grown in the presence of aspartic acid

From Figure 5-11, it is evident that as [Asp] increases in the crystal growth solution containing 10 mM Ca^{2+}, the percentage coverage increases. The largest increase in percentage coverage can be seen between crystals grown in 20 mM and 50 mM Asp. Crystals grown in 20 mM Asp and 1 mM Ca^{2+} have a percentage coverage similar to crystals grown in 20 mM Asp and 10 mM Ca^{2+} up until an exposure time of 120 mins. After this, the change in percentage coverage is marginal.

5.2.2.1.2 Glycine

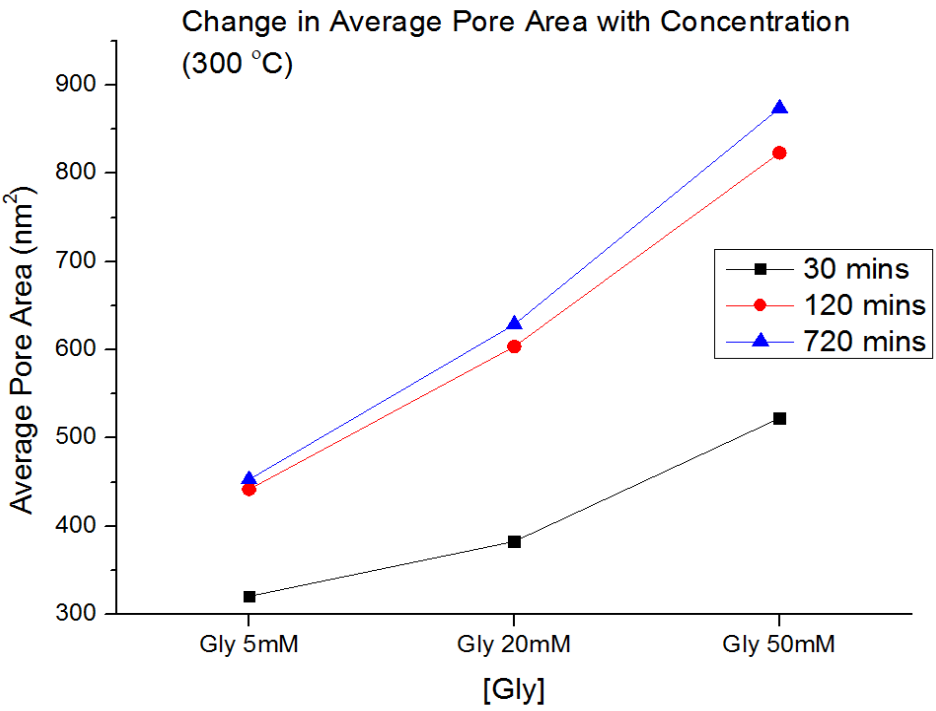

Figure 5-12: Change in pore area with concentration for calcite crystals grown in the presence of glycine

The change in pore area with increasing concentration of glycine is similar to that of crystals grown in the presence of Asp. This graph, in agreement with Figure 5-10, shows how the largest change in pore area occurs between exposure times of 30 minutes and 120 minutes. The largest pore areas are observed in crystals grown in 50 mM Gly.

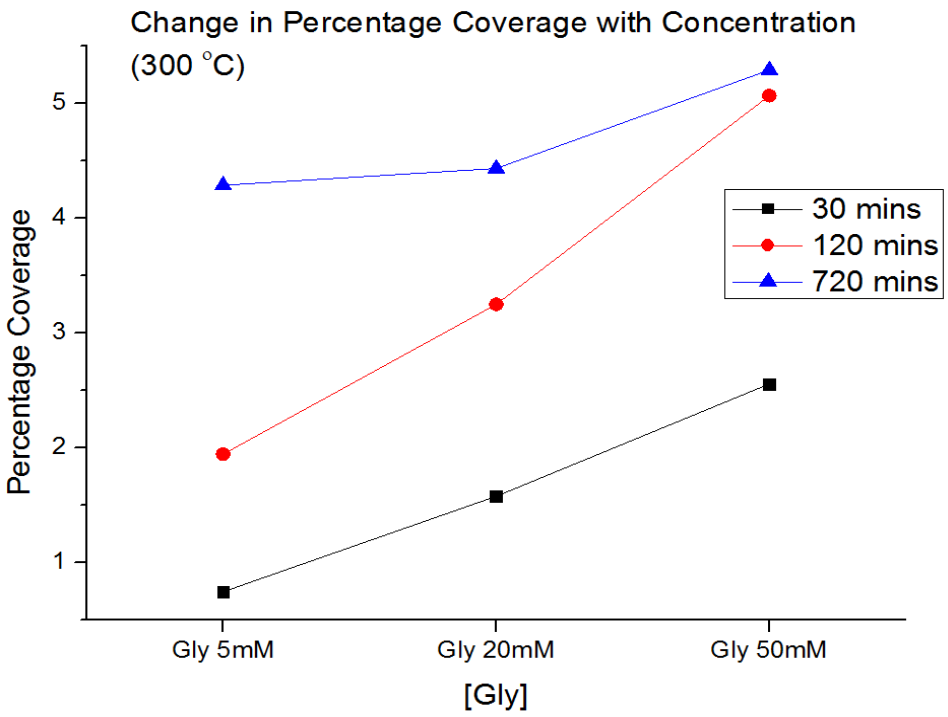

Figure 5-13: Change in percentage coverage with concentration for calcite crystals grown in the presence of glycine

The greatest percentage coverage is observed in samples grown in 50 mM Gly. The greatest change in percentage coverage is observed with increasing concentration with an exposure time of 120 mins at 300 °C.

5.2.2.2 Effect of annealing time on Pore Formation

5.2.2.2.1 Aspartic Acid

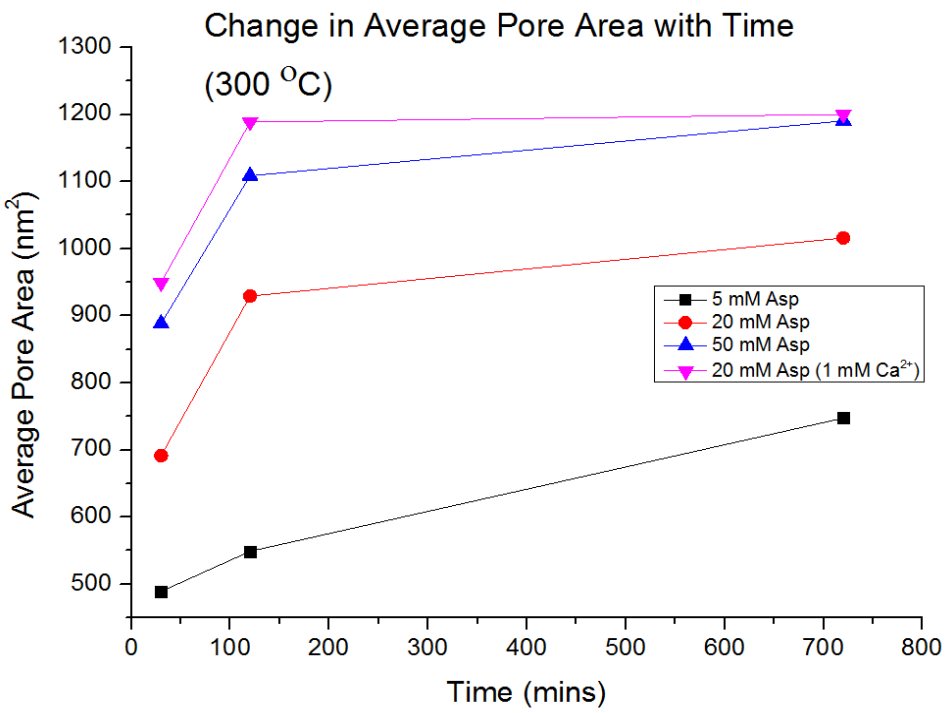

Figure 5-14: Change in pore area with time for calcite crystals grown in the presence of aspartic acid

This graph reinforces what is seen in Figure 5-10, in that the largest increase in pore area is observed between exposure times of 30 and 120 mins (with the exception of 5 mM Asp, in which the largest change is observed between 120 and 720 mins). It highlights the minute change in pore area between 120 and 720 mins in samples P3B, C and D.

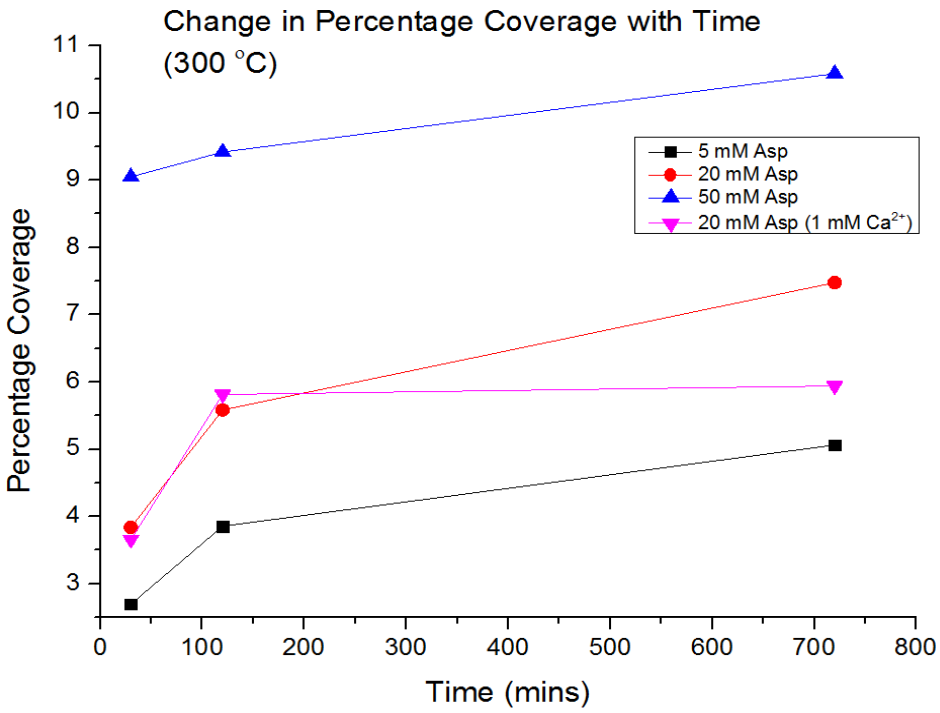

Figure 5-15: Change in percentage coverage with time for calcite crystals grown in the presence of aspartic acid

The greatest change in percentage coverage with time is witnessed between 30 and 120 mins, with the exception of P3C, in which a larger change is seen between 120 and 720 mins. The diminutive change in percentage coverage experienced by P3D between 120 and 720 mins is emphasised, especially when compared to the change that occurred for sample P3B, which was grown in the same concentration of Asp, but with a different [Ca^{2+}].

5.2.2.2.2 Glycine

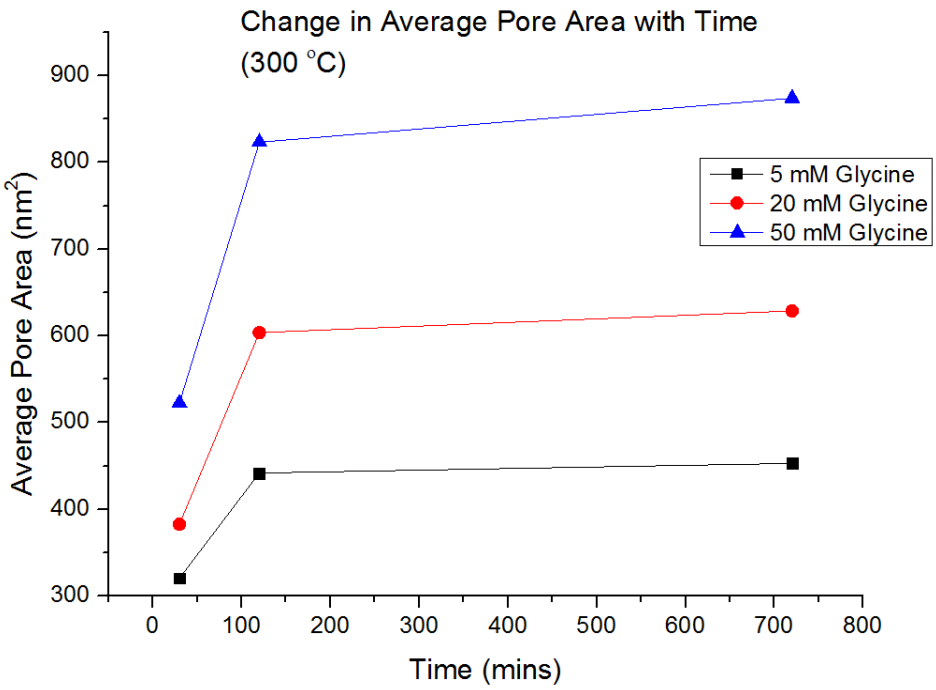

Figure 5-16: Change in average pore area with time for calcite crystals grown in the presence of glycine

Again, as seen in Figure 5-12, the largest change in average pore area is between 30 and 120 mins, with a small change occurring between 120 and 720 mins. The largest pore area is seen in crystals grown in the highest concentration of glycine.

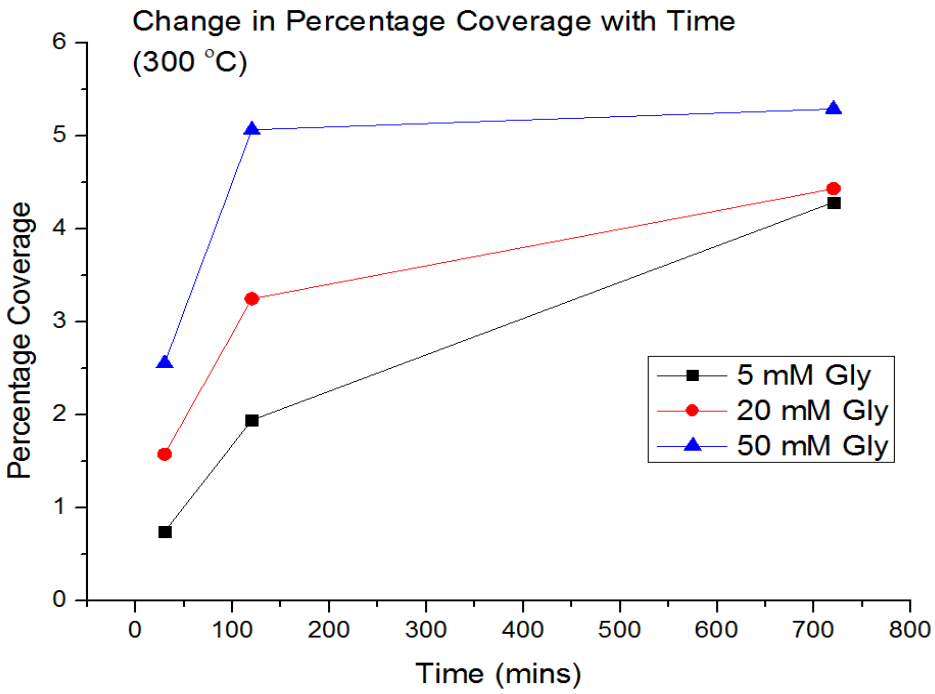

Figure 5-17: Change percentage coverage with time for calcite crystals grown in the presence of glycine

The information in this graph supports that of Figure 5-13. The greatest change in percentage coverage occurs between 30 and 120 mins and the largest percentage coverage is seen in the highest concentration of Gly.

5.2.3 Direct Observation of Pore Formation by TEM Using In-situ Heating Stage.

Samples of P3C (Asp 50 mM) and P3Z (Gly 5 mM) before heat treatment and P3C after exposure to 250 °C for 30 mins were chosen for TEM/Thermal stage analysis. The slow elevation of heat at 1 °C/min from room temperature to 400 °C was used to minimise drifting as a result of thermal expansion. The measured temperature was that of the sample holder and so the slow heating rate ensured that the sample would be at a similar temperature when images were taken every 10 °C. No pore formation or any processes indicating pore formation were observed for P3Z and so these images are excluded from this report.

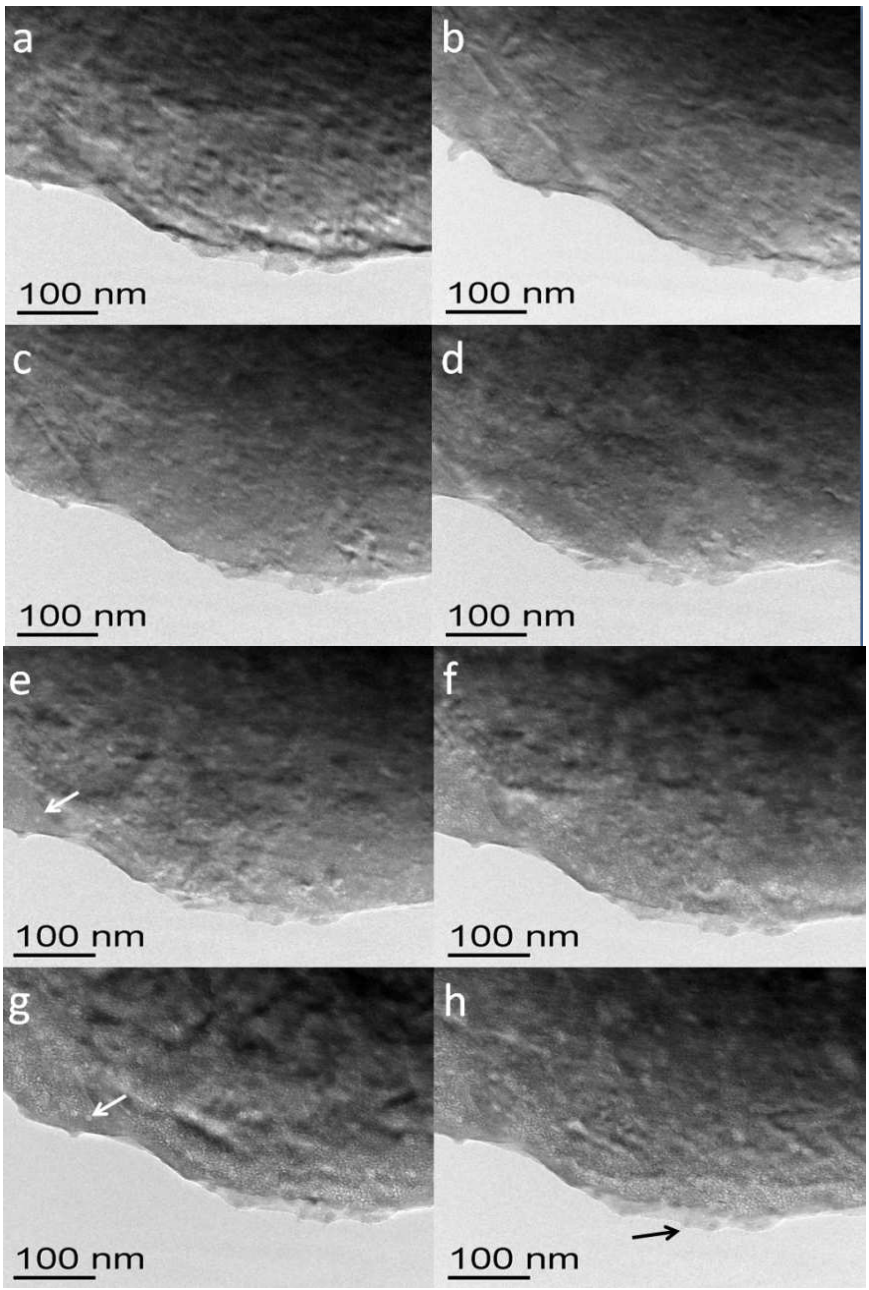
a
100 nm
b
100 nm
c
100 nm
d
100 nm
e
100 nm
f
100 nm
g
100 nm
h
100 nm

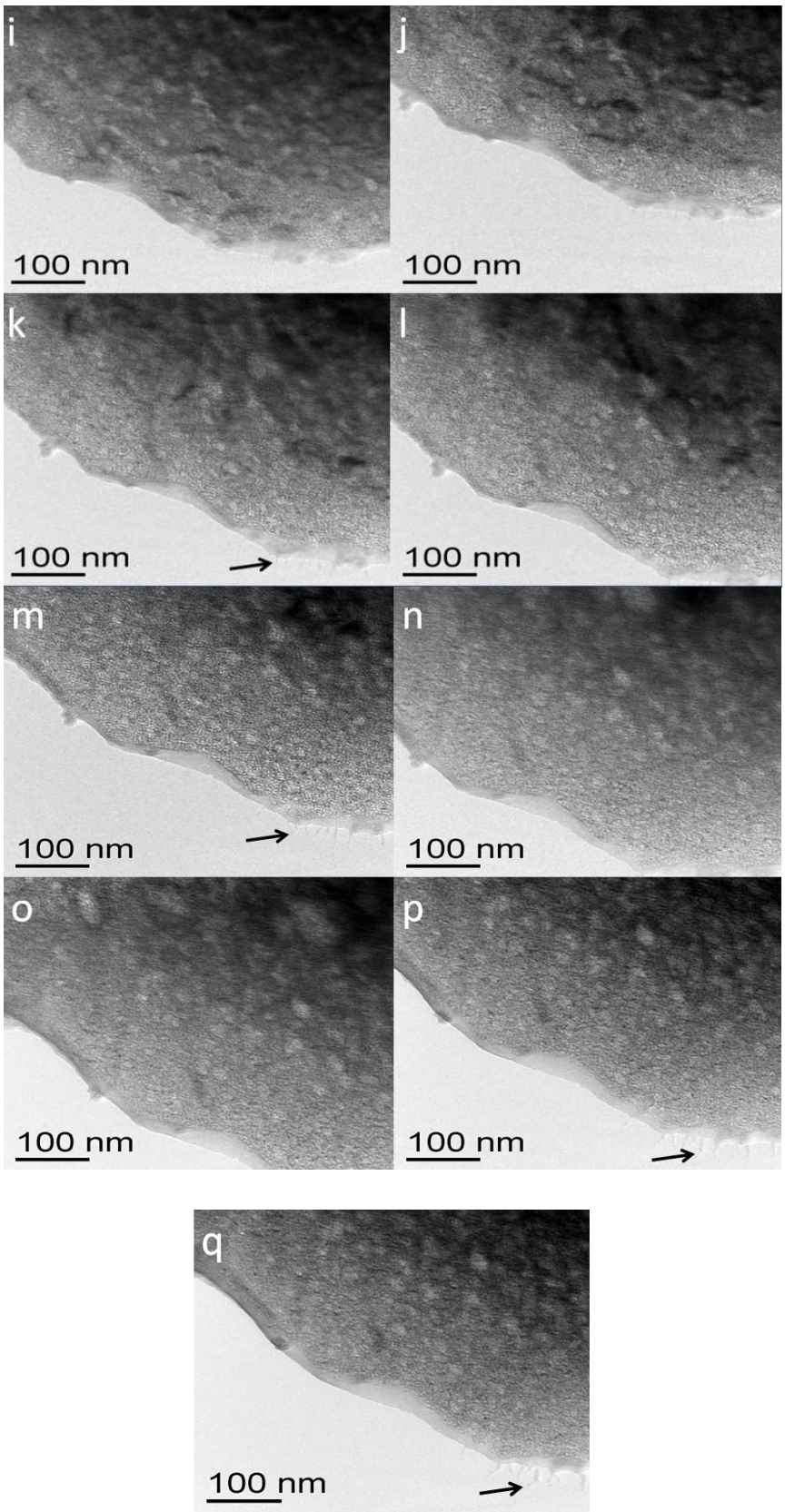

Figure 5-18: TEM/Thermal stage images of the same area (area 1) of a P3C crystal over a series of temperatures. The white arrows highlight pores, the black arrows highlight monocrystalline whiskers. (a) 25 °C (b) 50 °C (c) 70 °C (d) 120 °C (e) 140 °C (f) 150 °C (g) 160 °C (h) 170 °C (i) 190 °C (j) 200 °C (k) 220 °C (l) 240 °C (m) 260 °C (n) 280 °C (o) 315 °C (p) 350 °C (q) 402 °C.

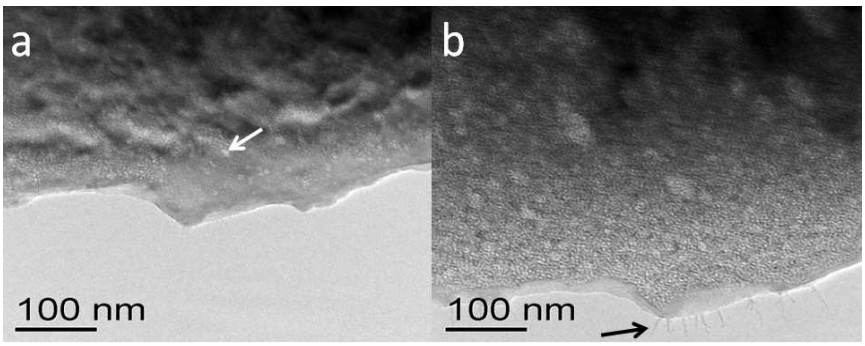

Figure 5-19: TEM/Thermal stage images of a different area (area 2) of the same P3C crystal as in area 1. These images were taken to highlight that pores and monocrystalline whiskers were also forming elsewhere. (a) 140 °C (b) 190 °C.

The TEM images from area one and two portray two simultaneous process occurring. The first is the formation of pores (individual pores are highlighted with the white arrows), which can be seen to start at 140 °C (e) and steadily increase in number and size (the largest was approximately 90 nm) up until 402 °C (q). The second is the development of what appear to be polycrystalline whiskers, first occurring at 170 °C as small 'stubs' and then progressively growing to a size of 20 nm (q). Pore and polycrystalline whisker formation was also observed in a different area of the same crystal (area 2). The pores and whiskers were of similar size to those found in area 2.

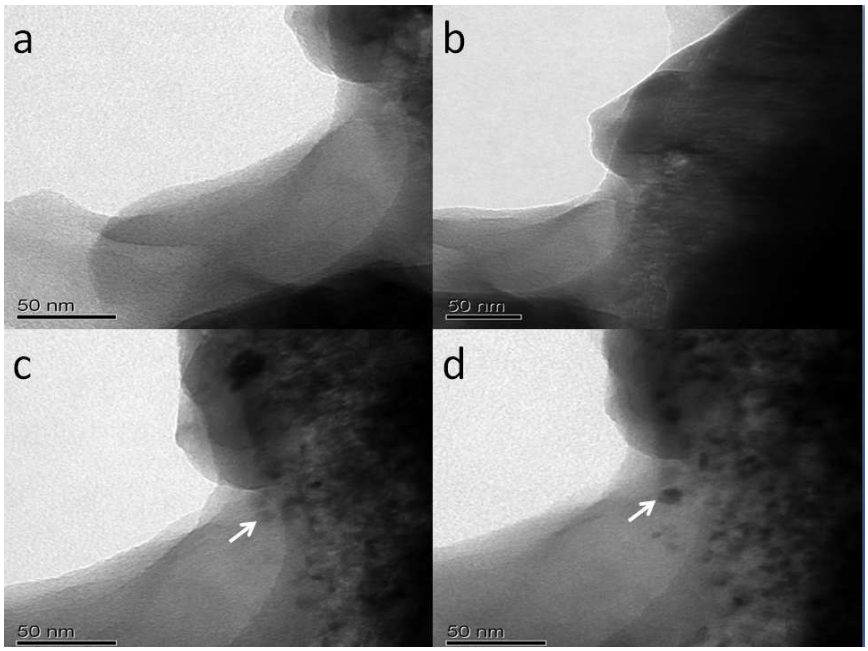

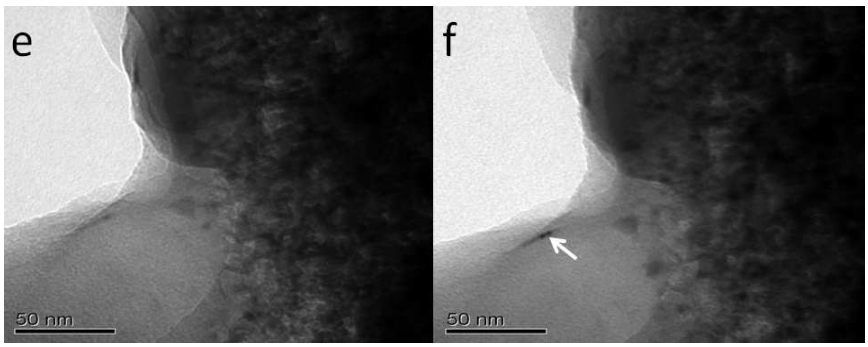

Figure 5-20: TEM/Thermal stage images of the same area of a P3C crystal that had been annealed at 250 °C for 30 mins prior to viewing. The white arrows indicate darker areas that could be due to recrystallisation. (a) 25 °C (b) 140 °C (c) 160 °C (d) 200 °C (e) 290 °C (f) 390

Figure 5-20 displays images of an area of a P3C crystal that had been annealed at 250 °C for 30 mins prior to viewing in the TEM. The white arrows highlights dark areas that were not present at room temperature and could be the result of recrystallisation processes.

5.2.4 Simultaneous TGA/IR Analysis

The FTIR spectra taken were through the mid infrared (4000 – 400 cm^{-1}). The TGA values were changed into percentage mass loss. The gain in mass of the samples is due to a buoyancy effect, which occurs as a result of a combination of true buoyancy effects, convection currents, gas flow drag effects, gas velocity effects, thermomolecular forces and thermal effects on the balance mechanism [96].

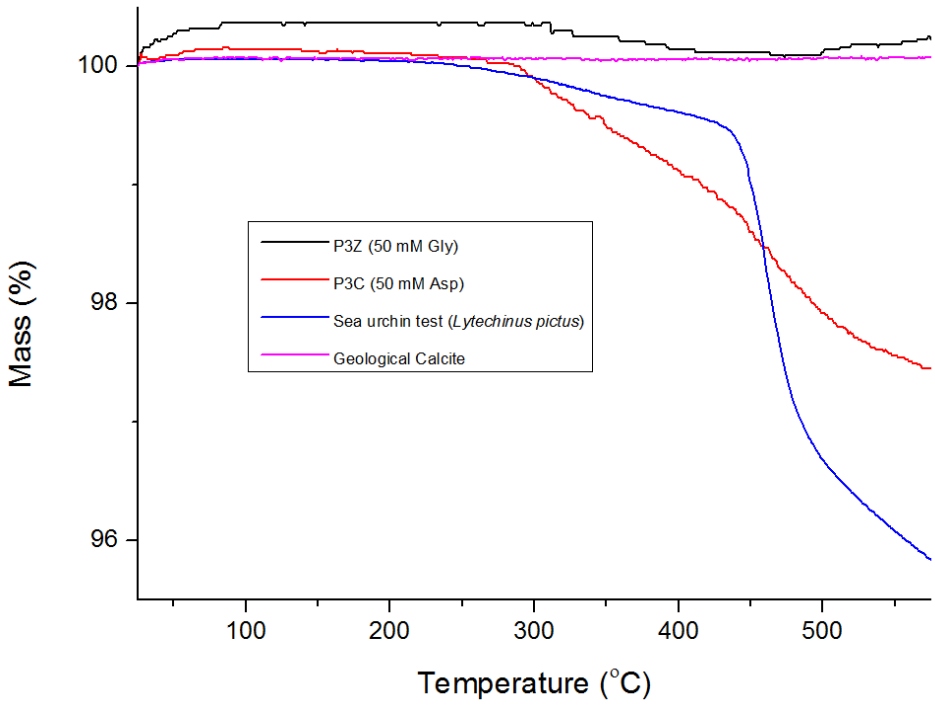

Figure 5-21: TGA traces from TGA/FTIR analysis of P3X, P3C, biomineral and geological calcite.

Figure 5-21 displays the TGA traces for the samples selected for TGA/FTIR analysis. The sea urchin biomineral calcite sample had experienced a percentage mass loss of 3.923 % by 550 °C, crystals grown in aspartic acid and glycine had lost 2.435 and 0 percentage mass loss respectively if the mass of the sample before the heating programme is used as the starting weight. However, if the starting mass value is taken as the maximum mass achieved during the heating programme, then the percentage mass loss is 4.642 % for biomineral calcite, 2.834 % for Asp calcite and 1.11293 % for Gly calcite. The decomposition of biomineral calcite up to 475 °C follows a two step process, with the first event beginning at 193.3 °C and the second at 428.5 °C. P3C follows a slightly different trend, in which there are three negative gradient changes (the first event is not very obvious in this figure, refer to Figure 5-25). The first decomposition event for P3C occurs at 181.7 °C, the second at 219.5 °C and the third at 434.3 °C. The mass losses in Gly calcite occur at 310.8 °C and a minor loss at 461.6 °C, with an unexplained mass gain at 497.9 °C. Geological calcite acts as a control and no mass loss is observed.

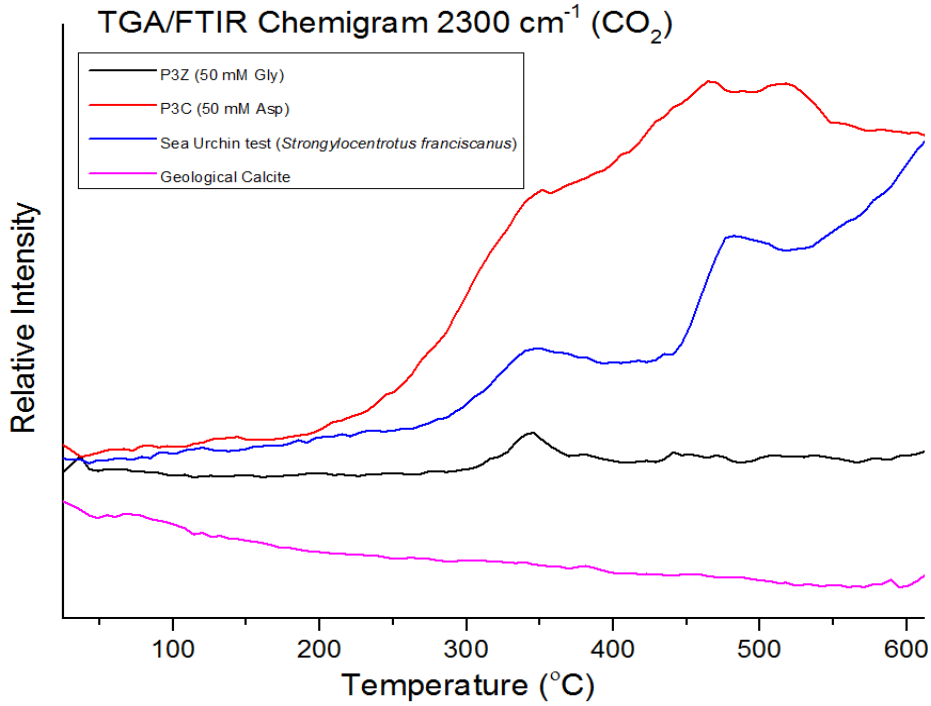

Figure 5-22: The chemigram obtained from TGA/FTIR taken at 2300 cm^{-1}, the region in which carbon dioxide is infrared active

Figure 5-22 provides a comparison between the chemigrams obtained at 2300 cm^{-1} for the various samples. A two step process can be seen with regards to the release of CO_2 from the sea urchin sample; beginning at approximately 275 ^{o}C and 440 ^{o}C. A similar, albeit less conspicuous two step process can be seen in the trace representing the 50 mM Asp sample, which starts at approx 200 ^{o}C and 360 ^{o}C. The Gly sample also produced a peak starting at 300 ^{o}C and 430 ^{o}C. The geological calcite sample was used as a control.

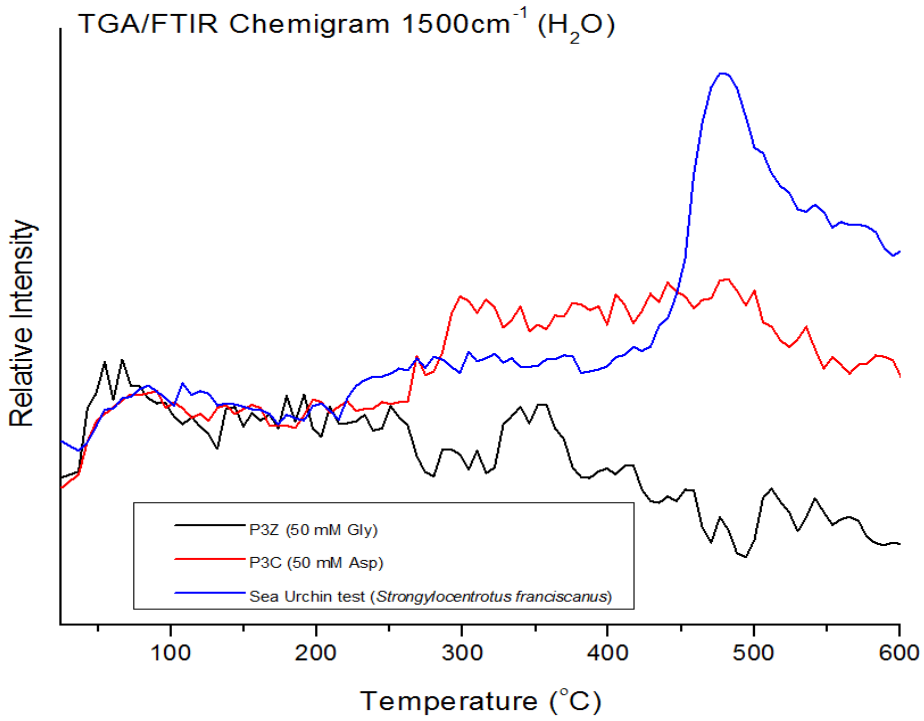

Figure 5-23: The chemigram obtained from TGA/FTIR taken at 1500 cm^{-1}, the region in which water is infrared active. The trace for geological calcite was removed as it flat lined.

Figure 5-23 provides a comparison between the chemigrams obtained at 1500 cm^{-1} for the various samples. The most prominent feature is the peak beginning at 422.8 ^{o}C in the sea urchin trace, which represents a large evolution of water until 480 ^{o}C, after which a decrease is observed. This peak is preceded by a smaller peak which begins at 215.4 °C. An emission of H_2O can also be seen in the P3C trace beginning at 262.3 ^{o}C, although not as pronounced as the second peak present in the sea urchin trace and the emission lasts until 505 ^{o}C after which it decreases. All three samples appear to release water between 40 and 125 ^{o}C, which is most probably H_2O that has just associated with the surface of the samples. The trace corresponding to P3X provides little information of use as a negative average gradient is present.

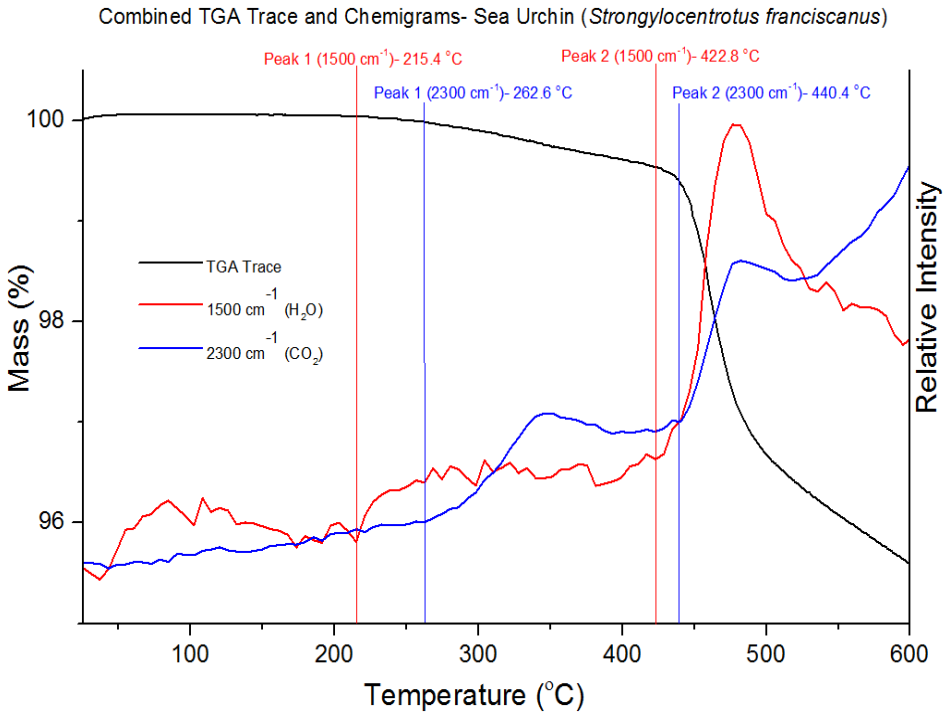

Figure 5-24: Combined TGA trace and chemigrams for the biomineral sample. The red lines indicate where the peaks begin with respect to the 1500 cm^{-1} chemigram and the blue lines with respect to the 2300cm^{-1} chemigram. These lines intersect with the TGA trace to highlight the change that occurs with respect to mass loss.

Figure 5-24 provides a comparison between the 1500 and 2300 cm^{-1} chemigrams and the TGA trace of biomineral calcite. A change in gradient of the TGA trace is associated with the onset of each peak. It appears that Peak 2 (1500 cm^{-1}) may have initiated a change in gradient, while Peak 2 (2300 cm^{-1}) added to it, as the gradient becomes more negative after passing.

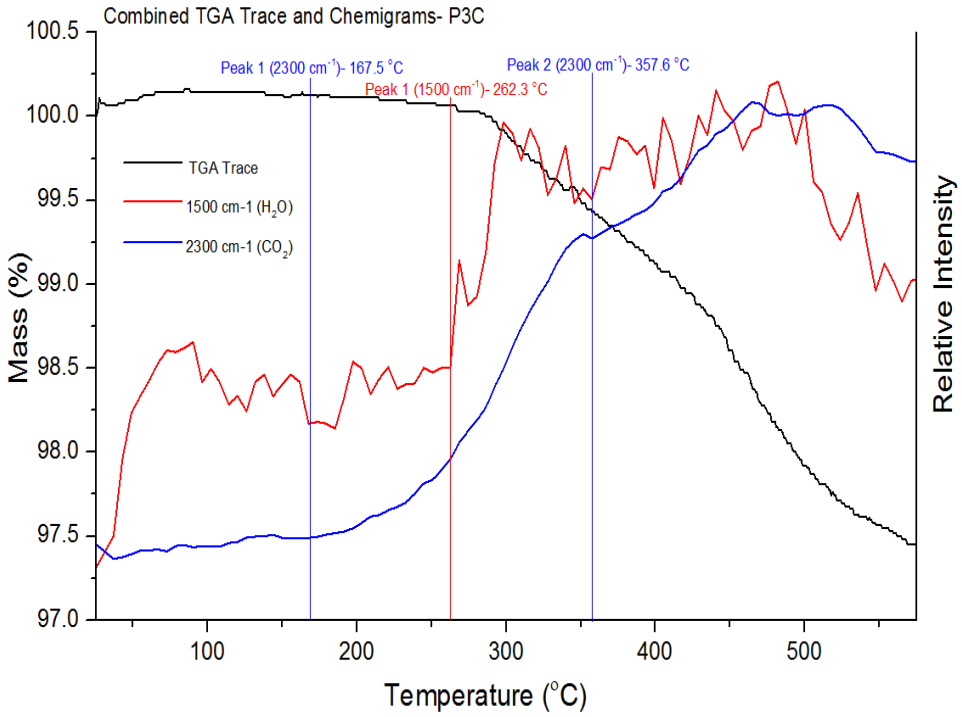

Figure 5-25: Combined TGA trace and chemigrams for P3C. The red lines indicate where the peaks begin with respect to the 1500 cm^{-1} chemigram and the blue lines with respect to the 2300cm^{-1} chemigram. These lines intersect with the TGA trace to highlight the change that occurs with respect to mass loss.

In Figure 5-25, a slight change in gradient occurs after Peak 1 (2300cm^{-1}) and a more pronounced alteration after Peak 1 (1500 cm^{-1}). A third change in gradient occurs after Peak 2 (2300 cm^{-1}) although with a delayed onset of approximately 70 ^{o}C.

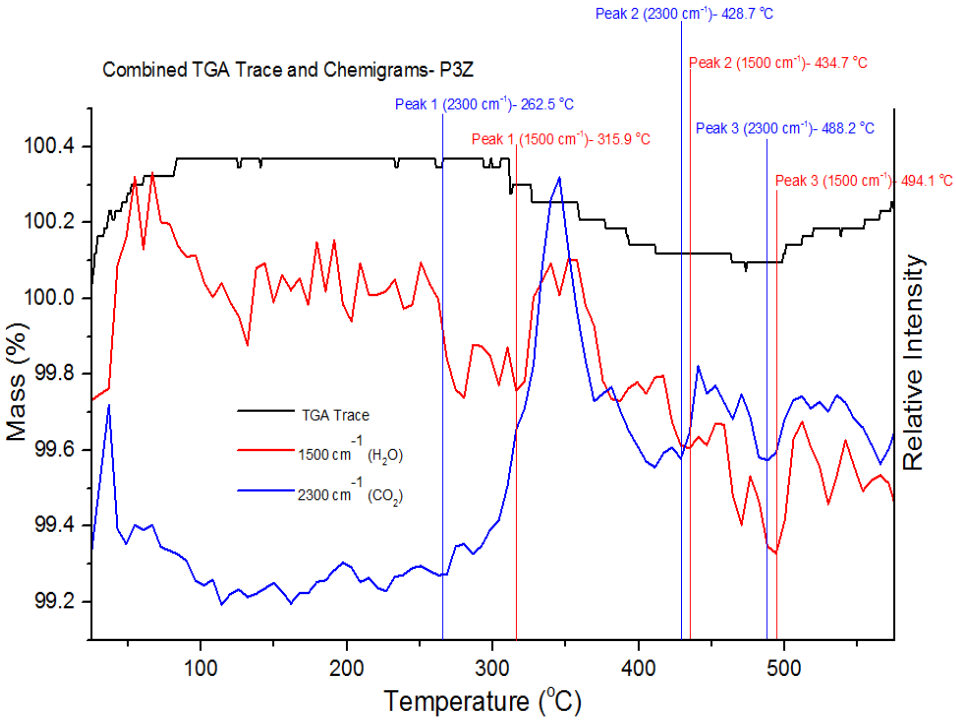

Figure 5-26: Combined TGA trace and chemigrams for P3Z. The red lines indicate where the peaks begin with respect to the 1500 cm^{-1} chemigram and the blue lines with respect to the 2300cm^{-1} chemigram. These lines intersect with the TGA trace to highlight the change that occurs with respect to mass loss.

In Figure 5-26, mass is lost from the sample after Peak 1 (2300 cm^{-1}), with a delayed onset of approximately 50 ^{o}C. Peak 1 (1500 cm^{-1}) then seems to add to this. The maxima of the Peak ones overlap. The Peak twos and threes overlap also, with a slight mass loss after the Peak twos and a mass gain after the Peak threes. The cause of this weight gain is unknown, as well as the first CO_2 peak (unlabelled) that begins at room temperature.

5.2.5 Surface Area and Density Analyses

Sample	***Surface Area of Sample (m^2/g)***
Geological Calcite	0.15
P3C (Asp 50 mM, Ca^{2+} 10 mM)	0.16

Table 5: Surface area measurements obtained for geological calcite and P3C (50 mM Asp)

6 Discussion

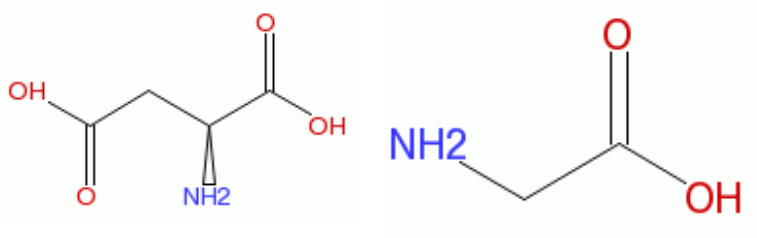

Figure 6-1: Structure of aspartic acid (left) [97], structure of glycine (right) [98].

Aspartic acid and glycine were the amino acids of choice due to their high levels of occlusion within calcite crystals, as proven by Borukhin *et al* [66]. Also, aspartic acid and glycine are commonly found as major components of macromolecules involved in biomineralisation and it is believed that they play a central role to the incorporation of these entities into the minerals, with continuous sequences of Asp residues found commonly [48], [68], [69], [70], [99]. That aspartic acid is negatively charged and glycine neutral provided a means to investigate how charge affected the nature of the pores formed upon annealing to high temperatures. Compared to the other naturally occurring amino acids, glycine is a small molecule and so the effect of the size of the occluded species on pore formation could also be considered. However, contrary to what would be expected, Borukhin *et al* observed relatively large lattice distortions induced by glycine, which could not be explained [66] (Section 2.2).

6.1.1 Crystal Morphology Analysis

The alteration to the morphology of the crystals can be explained with consideration of how the amino acid molecules interact with the growing crystals. The atomic steps of a pure calcite crystal reflect the symmetry of the {104} faces. There are four steps concerned with calcite crystal growth, two of which are acute to the {104} cleavage plane, the other two obtuse and each couple is related through a glide-plane symmetry element. The amino acids alter the shape of the bulk crystal through altering the energetics at the step edge. As observed by Orme *et al* [100], on addition of a racemic mixture of Asp, the acute steps become curved, while the obtuse steps are unaffected. Conversely, when a solution containing only one of the enantiomers is added (L-Asp with respect to this paper), the symmetry of the crystal system is reduced as the glide plane is broken. The addition of Asp produces a new low energy orientation for the acute step edges. This results in the

expression of a new set of facets that lie almost parallel to the <001> axis of pure calcite and map to the {hk0} plane family. The crystal undertakes a cylindrical morphology and is capped by three {104} facets; the unaffected obtuse steps are represented by the ridges joining the facets, and the acute steps correspond to the rounded base of the cap.

Figure 6-2: An SEM micrograph of a calcite crystal grown in 0.01M L-Asp by Orme *et al*. The rounded acute steps and the sharp obtuse steps can clearly be seen on the crystal.

According to Orme *et al*, an alteration of step velocity compared to that of the pure crystal indicates that an additive, such as Mg^{2+}, has been incorporated into the bulk crystal. It was postulated that Asp does not incorporate into the bulk of the calcite crystal, as the step velocity is largely independent of the concentration of Asp in solution. On the contrary, research carried out by Kim *et al* indicates that Asp molecules are present in the bulk of the crystal, as confirmed by high-resolution XRD. The data obtained indicated an expansion of the d spacing, and from this it was speculated that the large Asp molecule replaces two Ca^{2+} ions in the crystal lattice. This was also witnessed with Gly, although the d spacing wasn't as large, suggesting that Gly substitutes for one Ca^{2+} atom. The results from this study have not as of yet been published, and the association of these molecules with calcite remains an open-ended question.

6.1.2 Pore Morphology Analysis

The pores formed in all incidences were closed, as supported by the close similarity between the data obtained for the surface area analysis of geo calcite and P3C (Table 5). Also, the porous nature of the crystals was not apparent from surface inspection alone. It is evident that as the concentration of Asp increases, the shape of the pores changes from rhombi to a more circular form, and to a lesser extent in crystals grown in the presence of Gly. This is mirrored in the bulk morphology of the crystals and could be indicative of the nature of the association of the amino acids with the crystal lattice. At lower concentrations of Asp or with

Gly in general, if the amino acids assembled to form organic crystalline regions between nanodomains, then upon their removal, one would expect an irregularly shaped pore (which is not the case). This is because although the nanodomains may have a regular rhombohedral shape, upon removal of a number of them at random within the same region, an irregular shape on the larger scale would be formed. If however, the amino acids were part of the crystal lattice, then as they were released, the interactions between the remaining atoms that the amino acid was associated with would be less favourable and so these atoms would be more likely to leave the lattice as well and so the pore would be rhombohedral. On the contrary, the pores formed at higher concentrations of Asp favour the organic crystalline region/nanodomain theory, as the removal of nanodomains could allow the formation of spherical cavities, as spherical shapes minimize the surface free energy. It is speculated that high concentration of asp could be incorporated in the form of clusters, rather than individual molecules (see below).

6.1.3 Crystal Porosity Analysis

The mass loss of the samples is not solely down to the loss of biomolecules or amino acids, as confirmed by the chemigram taken at 1500 cm^{-1} (corresponding to water, Figure 5-23). It is likely that the amino acid and water molecules are associated with one another within the crystal. The fact that greater average pore density and percentage coverage is seen in crystals grown in Asp compared to Gly, along with the greater mass loss upon annealing, implies that Asp is incorporated more readily into the crystal than Gly.

As supported by the Image J analysis data, as the concentration of amino acid increases, the average pore area and percentage coverage also increases, with the exception of P3D (20 mM Asp, 1 mM Ca^{2+}). The P3D samples had the largest average pore area, but relatively low percentage coverage. This implies the presence of a size bias towards larger pores. After 120 minutes of exposure at 300 °C almost all of the pore forming agents had been removed from the crystal, as there was little change in average pore area or percentage coverage. An explanation for this could be that the lower concentration of Ca^{2+} results in a slower crystal growth rate. This in turn allows more time for Asp molecules to associate with each other to form clusters, perhaps through hydrogen bonds between the amide groups and carboxyl groups (if the organic crystalline/nanodomain argument is considered), before they become enclosed within the crystal. Upon heating to pore forming temperatures, the clusters of Asp are removed at a greater rate compared to the other Asp calcite samples as a result of their

association. This is supported by Figure 5-11 and Figure 5-15 because the sample (P3B) that has [Asp] comparable to P3D experiences an increase in percentage coverage from 120 to 720 minutes at 300 °C, whereas P3D does not. The association of Asp molecules into clusters within the crystal explains the larger pores seen in P3D compared to P3B, as well as the relatively low percentage coverage. The Image J data obtained for the crystals grown in the presence of Gly is more straightforward; the higher the concentration of Gly present in the solution, the more Gly is incorporated into the crystal and thus the average pore area and percentage coverage is greater for crystals grown in higher concentrations. After exposure to 300 °C for 120 minutes, a large portion of the occluded Gly has induced pore formation, and so little increase in average pore area and percentage coverage is observed between 120 and 720 minutes.

6.1.4 Pore Formation Analysis

The TEM/thermal stage images revealed that pore formation appears to occur at approximately 140 °C in a vacuous environment. In area one and two, a thinning of the crystal occurred simultaneously with pore formation and what appeared to be polycrystalline whiskers on the curved edges of the crystal. The TEM images of a P3C crystal that had previously been annealed revealed small regions of darker material that appeared above 160 °C and were not present in the image at room temperature. These observations further solidify that pore formation could be occurring as a result of a gaseous process, in that the gases that are released as the pores form are redistributed onto surface instabilities (the curved edges of the crystal where the polycrystalline whiskers formed). It is difficult to speculate exactly what material the darker regions were composed of, and XRD analysis could not be performed on the area as it was too small. However, it could be speculated that the material was crystalline as it originated from a single point (indicating nucleation). The whiskers are thought to be polycrystalline and not monocrystalline as they appear dendritic in form.

Due to the fact that the pores formed within the crystals are closed, it is possible that polycrystalline whiskers and a redistribution of material may occur on the surface of the pore. There was no evidence that gases had left the crystal, and polycrystalline whiskers were not observed on the external surface of the crystals.

From the Combined TGA Trace and Chemigram figures, the release of CO_2 and H_2O appear to overlap in all of the samples. This could be an indication that the release of the first chemical catalyses the release of the other. The first CO_2 event takes place at a much lower temperature in P3C than in P3Z, 167.5 °C and 262.5 °C respectively. This is unexpected, as it has been suggested that the association of Asp with the calcite lattice is likely to occur through the replacement of carbonate ions of the $(1\bar{1}0)$ plane with the carboxylate group of Asp, with these adsorbed molecules oriented parallel to the c-axis [99], [101]. Although the mechanism by which Gly molecules are associated with the calcite lattice remains undetermined, it would be assumed that the interactions between Gly molecules and the lattice would not be as strong as between Asp and the lattice, since Asp is an acidic amino acid and Gly neutral. However, the fact that carbon dioxide and water are evolved at lower temperatures in P3C than P3X may suggest that the interactions between the amino acids, water and the lattice are stronger in P3X, although further investigation would be required to confirm this.

In P3C and P3Z the release of CO_2 occurs before H_2O. It could be speculated that this is due to hydrogen bonding. Both Asp and water could form hydrogen bonds to the carbonate groups, although aspartic acid has more hydrogen bond donors than water (4 donors). The two hydrogen atoms of water are separated by an angle of 104.5°, while the only two hydrogen donors of aspartic acid situated next to each other (on the amine group) are separated by an angle of 107°, which more closely matches the bond angle between oxygen's in carbonate groups, 120°. However, the hydrogen bonds formed by the water molecule to the carbonate groups are likely to be stronger; as oxygen has a greater electron density than nitrogen, so is more electronegative. Also, water is a smaller molecule and therefore may be able to orient itself to form two hydrogen bonds more easily than aspartic acid. A similar situation is likely to occur in the case of glycine, as it is a bulkier molecule than water. In the sea urchin sample, H_2O evolution occurs before CO_2 evolution. This is probably due to the size of the macromolecules compared to the water molecules, which are much larger and so can form far more interactions per molecule. According to Seto *et al,* the mass loss between 200 and 550 °C corresponds to structural water leaving the bulk material [102] as well as when amorphous calcium carbonate transforms to crystalline calcite between 400 and 550 °C. This is confirmed by the IR spectra at 1500 cm^{-1} acquired in this experiment, although this data also implies that organic macromolecules leave with the water and the

greatest evolution of these molecules occurs as ACC transforms to calcite above 400 °C (Figure 5-24).

In Figure 5-22, a two step process occurs with regards to the release of CO_2 for the sea urchin sample. The two procedures could represent the different sizes of macromolecules associated with the sea urchin calcite; the first peak representing the smaller fraction. The peaks associated with CO_2 release for P3C and Z (2 for C and 3 for Z) could represent the different orientations and interactions that are possible between the amino acids and the crystal. Glycine is a smaller molecule and so more orientations may be possible. Furthermore, the Gly and sea urchin sample both released CO_2 at 262 °C; this could indicate that individual glycine molecules were present in the sea urchin sample.

7 Conclusions

Conclusions that can be drawn from this work are:

- Occlusions of Asp within calcite alter the morphology of the crystal much more than Gly occlusions. At high concentrations of Asp in the growth medium, the crystal fully departs the rhombohedral shape of the pure crystal and becomes a 'rugby ball' shape. At equivalent concentrations of Gly, the effect is much less noticeable. The alterations in morphology occur as a result of interactions between the amino acids and the step edge. Consequently, a new low energy step orientation occurs, causing a new set of facets to be expressed.
- Closed pores formed from annealing at 300 °C mirror the bulk morphology of the crystal. As the concentration of Asp increases, the shape of the pores progress from a rhombus shape at 5 mM to a circular/oval shape at 50 mM, independent of the duration of exposure to 300 °C. Longer exposure times and higher [Asp] results in larger pores and a greater density. In contrast, a change in pore shape with increasing [Gly] is not noticeable, but the density of pores and their size does increase with [Gly] and exposure time.
- With respect to samples grown in solutions of 10 mM Ca^{2+}, an increase in pore area was observed with increasing concentration of Asp. Crystals grown in 20 mM Asp and 1 mM Ca^{2+} displayed the largest pore areas, with values comparable to crystals grown in 50 mM Asp and 10 mM Ca^{2+}. This could be caused by the slow growth rate

of the crystals, allowing Asp molecules to associate into groups and then become trapped within the crystal.

- As [Asp] increases in the crystal growth solution containing 10 mM Ca^{2+}, the percentage coverage increases. The largest increase in percentage coverage was observed between crystals grown in 20 mM and 50 mM Asp. Crystals grown in 20 mM Asp and 1 mM Ca^{2+} have a percentage coverage similar to crystals grown in 20 mM Asp and 10 mM Ca^{2+} up until an exposure time of 120 mins. After this, the change in percentage coverage is marginal.
- The change in pore area with increasing concentration of glycine is similar to that of crystals grown in the presence of Asp. The largest change in pore area and percentage coverage occurs between exposure times of 30 minutes and 120 minutes. The largest pore areas and percentage coverage are observed in crystals grown in 50 mM Gly.
- Pore formation at lower temperatures observed in the vacuous environment of the TEM, the formation of polycrystalline whiskers and what appeared to be recrystallisation, indicate that a gaseous process is involved.
- A combination of organic decomposition and water evolution cause pore formation. The release of the first species may catalyse the release of the other. The greater average pore density and percentage coverage observed in Asp calcite compared to Gly, along with the greater mass loss upon annealing, implies that Asp is incorporated more readily into the crystal than Gly.
- The release of CO_2 before H_2O in the synthetic samples could indicate that water forms stronger interactions with the crystal than the amino acids as a result of its smaller size and more polarised paired hydrogen bond donors. H_2O evolution before CO_2 evolution in the sea urchin sample may be due to the greater number of interactions per molecule of macromolecule, due to their size, compared to water.

8 Future Work

Future plans to further the work described in this report would include:

1. Investigation into the effect of a wider variety of amino acids on the porosity of the calcite crystals. In addition, the result of homodimers and heterodimers of amino acids could be explored, as well as larger peptides. A wider range of concentrations of amino acids and Ca^{2+} could also be pursued.
2. TGA/mass spectrometry performed on the synthetic calcite crystals would identify structures of the organic gases evolved and the temperature at which they occur.
3. The regular and closed pores in single crystals could show interesting optical properties as it could scatter light in a very different manner compared to the solid form. This would be investigated.
4. The application of the same strategy described here to other crystals to see how universal this process is.

9 References

1. Shew, A., *Nanotech's History- An Interesting, Interdisciplinary, Ideological Split.* Bulletin of Science, Technology and Society, 2008. **28**(5): p. 390-399.
2. Sanchez, F. and K. Sobolev, *Nanotechnology in concrete- A review.* Construction and Building Materials, 2010. **24**(11): p. 2060-2071.
3. Shenhar, R. and V.M. Rotello, *Nanoparticles: scaffolds and building blocks.* Acc Chem Res, 2003. **36**(7): p. 549-61.
4. Lu, W. and M.L. Charles, *Nanoelectronics from the bottom up.* Nature Materials, 2007. **6**: p. 841-850.
5. Li, H., et al., *Microtubule Structure at 8 Angstrom Resolution.* Structure, 2002. **10**(10): p. 1317-1328.
6. Alberts, B., A. Johnson, and J. Lewis, *The Compartmentalization of Cells*, in *Molecular Biology of the Cell*2002, Garland Science: New York.
7. Lowenstam, H.A. and S. Weiner, *On Biomineralization*1989, New York: Oxford University Press.
8. Mann, S., *Biomineralization: principles and concepts in bioinorganic materials chemistry*. Oxford Chemistry Masters2001, Oxford: Oxford University Press.
9. Mukkamala, S.B., C.E. Anson, and A.K. Powell, *Modelling calcium carbonate biomineralisation processes.* Journal of Inorganic Biochemistry, 2006. **100**(5,Äì6): p. 1128-1138.
10. Livingston, B.T., et al., *A genome-wide analysis of biomineralization-related proteins in the sea urchin Strongylocentrotus purpuratus.* Developmental Biology, 2006. **300**(1): p. 335-348.
11. Watanabe, J.M. *Phylum Echinodermata: Subtidal Sea Urchins, Sea Cucumbers, & Brittle Stars* 2011; Available from: http://seanet.stanford.edu/EchinoHoloOphio/index.html.
12. Loban, C.S. *Current Research: Marine Benthic Diatom Biodiversity*. 2010; Available from: http://university.uog.edu/botany/lobban/lobban.htm.
13. Ehrlich, H., *Biological Materials of Marine Origin: Invertebrates*2010, London Springer London, Limited.
14. Seeman, N.C. and A.M. Belcher, *Emulating biology: Building nanostructures from the bottom up.* Proceedings of the National Academy of Sciences of the United States of America, 2002. **99**(Suppl 2): p. 6451-6455.
15. Stewart, J.J., *Application of the PM6 method to modeling the solid state.* J Mol Model, 2008. **14**(6): p. 499-535.
16. Weiner, S. and P.M. Dove, *An overview of biomineralization processes and the problem of the vital effect.* Reviews in Mineralogy and Geochemistry, 2003. **54**(1): p. 1-29.
17. Federation, B.C.C. *Calcium Carbonate- An Exceptional Mineral*. 2007.
18. Xiang, L., et al., *Formation of CaCO3 nanoparticles in the presence of terpineol.* Materials Letters, 2004. **58**(6): p. 959-965.
19. Tegethoff, F.W., J.W. Rohleder, and E. Kroker, *Calcium carbonate: from the Cretaceous period into the 21st century*2001, Basel: Springer
20. Kelly, A.A. and K.M. Knowles, *Crystallography and Crystal Defects*. 2 ed2012, Chichester: John Wiley & Sons.

21. Baer, D.R. and D.L. Blanchard Jr, *Studies of the calcite cleavage surface for comparison with calculation.* Applied Surface Science, 1993. **72**(4): p. 295-300.
22. Gorr, M.C., *An atomic force microscope (AFM) study of the calcite cleavage plane: Image averaging in Fourier space.* American Mineralogist, 1992. **77**: p. 904-910.
23. Reddy, M.M. and A.R. Hoch, *Calcite crystal growth rate inhibition by polycarboxylic acids.* Journal of colloid and interface science, 2001. **235**(2): p. 365-370.
24. Reddy, M.M. and G.H. Nancollas, *Calcite crystal growth inhibition by phosphonates.* Desalination, 1973. **12**(1): p. 61-73.
25. Lowenstam, H., *Magnetite in Denticle Capping in Recent Chitons (Polyplacophora).* Geological Society of America Bulletin, 1962. **73**(4): p. 435-438.
26. Politi, Y., et al., *Transformation mechanism of amorphous calcium carbonate into calcite in the sea urchin larval spicule.* Proceedings of the National Academy of Sciences, 2008. **105**(45): p. 17362-17366.
27. Weiner, S., I. Sagi, and L. Addadi, *Choosing the crystallization path less traveled.* Science, 2005. **309**(5737): p. 1027-1028.
28. Beniash, E., et al., *Amorphous calcium carbonate transforms into calcite during sea urchin larval spicule growth.* Proceedings of the Royal Society of London. Series B: Biological Sciences, 1997. **264**(1380): p. 461-465.
29. Addadi, L., S. Raz, and S. Weiner, *Taking advantage of disorder: amorphous calcium carbonate and its roles in biomineralization.* Advanced Materials, 2003. **15**(12): p. 959-970.
30. Hasse, B., et al., *Calcium carbonate modifications in the mineralized shell of the freshwater snail Biomphalaria glabrata.* Chemistry-A European Journal, 2000. **6**(20): p. 3679-3685.
31. Sommerdijk, N.A., *Biomimetic CaCO3 mineralization using designer molecules and interfaces.* Chemical reviews, 2008. **108**(11): p. 4499.
32. Carpenter, K.J. and W.M.L. Wood, *Industrial crystallization for fine chemicals.* Advanced Powder Technology, 2004. **15**(6): p. 657-672.
33. Yu, Z.Q., et al., *Recent Advances in Crystallization control: An Industrial Perspective.* Chemical Engineering Research and Design, 2007. **85**(7): p. 893-905.
34. Cohen, P.A., et al., *Phosphate biomineralization in mid-Neoproterozoic protists.* Geology, 2011. **39**(6): p. 539-542.
35. De Yoreo, J. and P.G. Vekilov, *Principles of Crystal Nucleation and Growth*, in *Biomineralization*, P.M. Dove, J. De Yoreo, and S. Weiner, Editors. 2003, Mineralogical Society of America. p. 57-93.
36. Verma, A.R., *Polymorphism and Polytypism in Crystals* 1966, New York: John Wiley & Sons Inc.
37. Byrappa, K. and T. Ohachi, *Crystal Growth Technology*2002, New York: William Andrew Publishing.
38. Mullin, J.W., *Crystallization*2001, Oxford: Butterworth-Heinemann.
39. Krebs, H., *Fundamentals of Inorganic Crystal Chemistry*1968, London: McGraw-Hill.
40. Verma, A.R., *Crystal Growth and Dislocations*. 1 ed1953, London: Butterworths Scientific. 182.
41. Tiller, W.A., *The Science of Crystallization*1991, Cambridge: Cambridge University Press. 391.
42. Davey, R. and J. Garside, *From Molecules to Crystallizers: An Introduction to Crystallization*2006, Oxford: Oxford University Press.
43. Sunagawa, I., *Crystals: Growth, Morphology and Perfection*2005, Cambridge: Cambridge University Press.

44. Shchukin, V., N.N. Ledentsov, and D. Bimberg, *Epitaxy of Nanostructures*. Nanoscience and TEchnology, ed. P. Avouris, et al.2004, Berlin: Springer.
45. Cubillas, P. and M.W. Anderson, *Synthesis Mechanism: Crystal Growth and Nucleation*, in *Zeolites and Catalysis*2010, Wiley-VCH Verlag GmbH & Co. KGaA. p. 1-55.
46. Towe, K.M. and G.R. Thompson, *The structure of some bivalve shell carbonates prepared by ion-beam thinning.* Calcified tissue research, 1972. **10**(1): p. 38-48.
47. Berman, A., L. Addadi, and S. Weiner, *Interactions of sea-urchin skeleton macromolecules with growing calcite crystals- a study of intracrystalline proteins.* Nature, 1988. **331**: p. 546-548.
48. Li, H., et al., *Calcite Prisms from Mollusk Shells (Atrina Rigida): Swiss-cheese-like Organic–Inorganic Single-crystal Composites.* Advanced Functional Materials, 2011. **21**(11): p. 2028-2034.
49. Sethmann, I., et al., *Nano-cluster composite structure of calcitic sponge spicules- a case study of basic characteristics of biominerals.* Journal of Inorganic Biochemistry, 2006. **100**(1): p. 88-96.
50. Rousseau, M., et al., *Multiscale structure of sheet nacre.* Biomaterials, 2005. **26**(31): p. 6254-6262.
51. Mann, S., *Biomineralization: principles and concepts in bioinorganic materials chemistry*2001, Oxford: Oxford University Press, Incorporated.
52. Weiner, S. and L. Addadi, *Acidic macromolecules of mineralized tissues: The controllers of crystal formation.* Trends in Biochemical Sciences, 1991. **16**(0): p. 252-256.
53. Veis, A. and A. Perry, *The Phosphoprotein of the Dentin Matrix.* Biochemistry, 1967. **6**(8): p. 2409-2416.
54. Herring, G.M., *Comparison of bovine bone sialoprotein and serum orosomucoid.* Nature, 1964. **201**: p. 709.
55. Zamoscianyk, H. and A. Veis, *The isolation and chemical characterization of a phosphate-containing siaglycoprotein from developing bovine teeth.* Fedn Proc. Fedn Am. Socs exp. Biol, 1966. **25**: p. 409.
56. Schlueter, R.J. and A. Veis, *The Macromolecular Organization of Dentine Matrix Collagen. II. Periodate Degradation and Carbohydrate Cross-Linking.* Biochemistry, 1964. **3**(11): p. 1657-1665.
57. Weiner, S., W. Traub, and H.A. Lowenstam, *Organic matrix in calcified exoskeletons.* 1982: p. 205-224.
58. Weiner, S. and H. Lowenstam, *Organization of Extracellularly Mineralized Tissues: A Comparative Study of Biological Crystal Growth.* Critical Reviews in Biochemistry and Molecular Biology, 1986. **20**(4): p. 365-408.
59. Addadi, L., et al., *A chemical model for the cooperation of sulfates and carboxylates in calcite crystal nucleation: relevance to biomineralization.* Proceedings of the National Academy of Sciences, 1987. **84**(9): p. 2732-2736.
60. Addadi, L. and S. Weiner, *Interactions between acidic proteins and crystals: stereochemical requirements in biomineralization.* Proc Natl Acad Sci U S A, 1986. **82**(12): p. 4110-4.
61. Mann, S., *Molecular recognition in biomineralization.* Nature, 1988. **332**(6160): p. 119-124.
62. Berman, A., et al., *Total alignment of calcite at acidic polydiacetylene films: cooperativity at the organic-inorganic interface.* Science, 1995. **269**(5223): p. 515-518.

63. Dauphin, Y., *Soluble organic matrices of the calcitic prismatic shell layers of two Pteriomorphid bivalves. Pinna nobilis and Pinctada margaritifera.* J Biol Chem, 2003. **278**(17): p. 15168-77.
64. Albeck, S., et al., *Interactions of various skeletal intracrystalline components with calcite crystals.* Journal of the American Chemical Society, 1993. **115**(25): p. 11691-11697.
65. Gotliv, B.-A., et al., *Asprich: A Novel Aspartic Acid-Rich Protein Family from the Prismatic Shell Matrix of the Bivalve Atrina rigida.* ChemBioChem, 2005. **6**(2): p. 304-314.
66. Borukhin, S., et al., *Screening the Incorporation of Amino Acids into an Inorganic Crystalline Host: the Case of Calcite.* Advanced Functional Materials, 2012. **22**(20): p. 4216-4224.
67. Aizenberg, J., et al., *Factors involved in the formation of amorphous and crystalline calcium carbonate: a study of an ascidian skeleton.* J Am Chem Soc, 2002. **124**(1): p. 32-9.
68. Weiner, S. and L. Hood, *Soluble protein of the organic matrix of mollusk shells: a potential template for shell formation.* Science, 1975. **190**(4218): p. 987-989.
69. Weiner, S., *Mollusk shell formation: isolation of two organic matrix proteins associated with calcite deposition in the bivalve Mytilus californianus.* Biochemistry, 1983. **22**(17): p. 4139-4145.
70. Weiner, S., *Organization of organic matrix components in mineralized tissues.* American zoologist, 1984. **24**(4): p. 945-951.
71. Chernov, A.A., et al., *Modern Crystallography III: Crystal Growth*. Reprint ed2011, London: Springer.
72. Uhlmann, D.R., B. Chalmers, and K.A. Jackson, *Interaction Between Particles and a Solid-Liquid Interface.* Journa of Applied Physics, 1964. **35**: p. 2986-2994.
73. Omenyi, S.N., et al., *Attraction and repulsion of solid particles by solidification fronts II. Dimensional analysis.* Journal of Applied Physics, 1981. **52**(796): p. 789-95.
74. Kim, Y.-Y., et al., *Bio-Inspired Synthesis and Mechanical Properties of Calcite–Polymer Particle Composites.* Advanced Materials, 2010. **22**(18): p. 2082-2086.
75. Li, H. and L.A. Estroff, *Calcite Growth in Hydrogels: Assessing the Mechanism of Polymer-Network Incorporation into Single Crystals.* Advanced Materials, 2009. **21**(4): p. 470-473.
76. Marentette, J.M., et al., *Crystallization of CaCO3 in the presence of PEO-block-PMAA copolymers.* Advanced Materials, 1997. **9**(8): p. 647-651.
77. Lu, C., et al., *Synthesis of Calcite Single Crystals with Porous Surface by Templating of Polymer Latex Particles.* Chem. Mater, 2005. **17**: p. 5218-5224.
78. Berman, A., et al., *Intercalation of sea urchin proteins in calcite: study of a crystalline composite material.* Science, 1990. **250**(4981): p. 664-7.
79. Young, J.R., et al., *Coccolith Ultrastructure and Biomineralisation.* Journal of Structural Biology, 1999. **126**(3): p. 195-215.
80. Kim, Y.-Y., et al., *An artificial biomineral formed by incorporation of copolymer micelles in calcite crystals.* Nature Materials, 2011. **10**(11): p. 890-896.
81. Hetherington, N.B.J., et al., *Crystallization on Surfaces of Well-Defined Topography.* Langmuir, 2005. **22**(5): p. 1955-1958.
82. Li, C. and L. Qi, *Bioinspired Fabrication of 3D Ordered Macroporous Single Crystals of Calcite from a Transient Amorphous Phase.* Angewandte Chemie International Edition, 2008. **47**(13): p. 2388-2393.

83. Li, H. and L.A. Estroff, *Porous calcite single crystals grown from a hydrogel medium.* CrystEngComm, 2007. **9**(12): p. 1153-1155.
84. Park, R.J. and F.C. Meldrum, *Synthesis of Single Crystals of Calcite with Complex Morphologies.* Advanced Materials, 2002. **14**(16): p. 1167-1169.
85. Meldrum, F.C. and S. Ludwigs, *Template-Directed Control of Crystal Morphologies.* Macromolecular Bioscience, 2007. **7**(2): p. 152-162.
86. Yue, W., A.N. Kulak, and F.C. Meldrum, *Growth of single crystals in structured templates.* Journal of Materials Chemistry, 2006. **16**(4): p. 408-416.
87. Park, R.J. and F.C. Meldrum, *Shape-constraint as a route to calcite single crystals with complex morphologies.* Journal of Materials Chemistry, 2004. **14**(14): p. 2291-2296.
88. Jimmy, C., *Facile fabrication and characterization of hierarchically porous calcium carbonate microspheres.* Chemical communications, 2004(21): p. 2414-2415.
89. Walsh, D., et al., *Synthesis of Macroporous Calcium Carbonate/Magnetite Nanocomposites and their Application in Photocatalytic Water Splitting.* Small, 2011. **7**(15): p. 2168-2172.
90. Yu, H.-D., S.Y. Tee, and M.-Y. Han, *Preparation of porosity-controlled calcium carbonate by thermal decomposition of volume content-variable calcium carboxylate derivatives.* Chemical Communications, 2013. **49**(39): p. 4229-4231.
91. Gehrke, N., et al., *Superstructures of Calcium Carbonate Crystals by Oriented Attachment.* Crystal Growth & Design, 2005. **5**(4): p. 1317-1319.
92. Zuykov, M., et al., *In vitro growth of calcium carbonate crystals on bivalve shells: Application of two methods of synthesis.* Materials Science and Engineering: C, 2012. **32**(5): p. 1158-1163.
93. Schenk, A.S., et al., *Impurities in pluronic triblock copolymers can induce the formation of calcite mesocrystals.* Chemical Geology, 2012. **294-295**: p. 259-262.
94. Kendall, D.N., *Identification of Polymorphic Forms of Crystals by Infrared Spectroscopy.* Analytical Chemistry, 1953. **25**(3): p. 382-389.
95. Freeman, S.K., *Applications of Laser Raman Spectroscopy*1974, New York: John Wiley & Sons. 336.
96. THASS. *Buoyancy Phenomenon in TGA Systems*. 2012; Available from: http://www.thass.org/DOWN/applications/TGA%20Applications/pdfthass/chn206%20Buoancy.pdf.
97. Inc, e. *Structure of Aspartic Acid*. 2013.
98. Inc, e. *Structure of Glycine*. 2013; Available from: https://www.emolecules.com/cgi-bin/more?vid=483675.
99. Wierzbicki, A., et al., *Atomic force microscopy and molecular modeling of protein and peptide binding to calcite.* Calcified Tissue International, 1994. **54**(2): p. 133-141.
100. Orme, C.A., et al., *Formation of chiral morphologies through selective binding of amino acids to calcite surface steps.* Nature, 2001. **411**(6839): p. 775-779.
101. Mann, S., et al., *Morphological influence of functionalized and non-functionalized [small alpha],[small omega]-dicarboxylates on calcite crystallization.* Journal of the Chemical Society, Faraday Transactions, 1990. **86**(10): p. 1873-1880.
102. Seto, J., et al., *Structure-property relationships of a biological mesocrystal in the adult sea urchin spine.* Proceedings of the National Academy of Sciences, 2012. **109**(10): p. 3699-3704.